ICARUS 113, 360–386 (1995)

Images of Pluto Generated by Matrix Lightcurve Inversion

WILLIAM F. DRISH, JR.

5159 West 64th Place, Chicago, Illinois 60638

ROBERT HARMON[1]

Department of Physics and Enrico Fermi Institute, University of Chicago, 5640 South Ellis Avenue, Chicago, Illinois 60637

ROBERT L. MARCIALIS

Lunar and Planetary Laboratory, University of Arizona, Tucson, Arizona 85721

AND

WALTER J. WILD

Department of Astronomy and Astrophysics, University of Chicago, 5640 South Ellis Avenue, Chicago, Illinois 60637
E-mail: walter@babylon.uchicago.edu

Received February 22, 1994; revised August 15, 1994

We use a new indirect imaging method, matrix lightcurve inversion (MLI), to generate surface albedo maps of Pluto from the rotational photometric lightcurves. The mathematical basis of MLI is established and a constrained iterative regularization method used to invert the underdetermined system of equations. If the secular dimming of Pluto observed in all phases of the rotational lightcurves from 1954 to 1982, followed by an overall brightening of the planet in later years, could be ascribed to a static surface albedo distribution, then an albedo map can be generated using all the available lightcurves. However, Stern *et al.* (1988, *Icarus* 75, 485–498) have suggested that an extensive covering of methane frost sublimates as Pluto approaches perihelion, exposing dark layers of photolyzed methane in a spatially nonuniform pattern, and then freezes out again as Pluto passes perihelion. Assuming that Stern *et al.* (1988, *Icarus* 75, 485–498) are correct in their interpretation that Pluto undergoes atmospheric sublimation and freezeout cycles, we present an image that represents a *snapshot* of Pluto as it might have appeared during the interval 1980 to 1986 by using lightcurves measured in these years. Another image using the lightcurves between 1954 and 1986 shows very extensive and bright polar caps though this image appears to be highly unrealistic. We propose that the inability to fit these lightcurves (to even remotely within the noise level in the data) furnishes evidence to the hypothesis of large-scale and dynamic atmospheric volatile transport over Pluto's surface between the mid 1950s and the mid 1980s.

INTRODUCTION

Pluto is the smallest planetary member of the known Solar System. With a diameter of ~2300 km and mean heliocentric distance of ~40 AU, the disk of the planet subtends approximately 0.1″ (Stern 1992). It has thus far been impossible to resolve any details on Pluto's surface and even the HST cannot render more than ~3 resolution pixels across the planet's surface at visible wavelengths. Consequently, images of the Pluto–Charon system are primarily used for astrometric and barycentric analyses of the system (see for example, Null *et al.* 1993), to refine mass and density estimates for the two bodies, and to acquire individual lightcurves and spectra. Pluto exhibits a rotational and orbital lightcurve which contains valuable information about the surface scattering or albedo distribution (Marcialis 1988). These lightcurves can be inverted to generate images of the surface of Pluto which satisfy the lightcurve constraints. Lightcurve inversion is a superresolution, i.e., indirect, imaging technique that can be used to infer surface albedo distributions, pole orientations, and three-dimensional shapes for planets and their satellites, and asteroids, and can be used to map the brightness distribution of magnetically active spotted stars (Rodono 1986) and contact–binary stars such as RS CVn variable stars (Eaton and Hall 1979).

Russell (1906) first considered the potentialities of lightcurve inversion. He concluded that lightcurve inversion via spherical harmonics decomposition was an ill-

[1] Present address: Department of Physics, Randolph–Macon College, P.O. Box 5005, Ashland, VA 23005-5505.

0019-1035/95 $6.00

posed method because all of the odd harmonic components beyond the first do not contribute to the frequency content of a lightcurve (see also Magnusson *et al.* 1989). Consequently, an infinite number of brightness distributions and/or shapes may satisfy a lightcurve. The greatest ambiguity occurs when only one lightcurve is measured from an equatorial view at zero solar phase angle. For several decades investigators appeared to have been deterred by Russell's analysis of lightcurve inversion until Lacis and Fix (1971) applied the spherical harmonics formalism to the asteroids 4 Vesta and 39 Laetitia. Attempts to map Pluto's albedo distribution using Fourier methods were made by Lacis and Fix (1972) and Renschen (1977), but these efforts were severely hampered by a lack of accurate knowledge of Pluto's pole position, and by being constrained to use only the lowest spherical harmonics in the lightcurve expansion. Andersson and Fix (1973) employed an adaptation of Russell's Fourier technique to derive what turned out to be a fair estimate of Pluto's pole position, but they did not attempt to determine an albedo distribution. The subsequent discovery of Pluto's satellite Charon (Christy and Harrington 1978) yielded a reasonably accurate pole position. At about the same time, the increasing availability of computers made the numerical simulation of lightcurves tractable. Marcialis (1983) first applied simple spot modeling techniques to the Pluto problem. Subsequently, a host of papers appeared in which further computational complexity was added to the inversion of Pluto's rotational lightcurves and mutual event data (cf. Marcialis 1988, Buie and Tholen 1989, Buie *et al.* 1992; Young and Binzel 1989, 1990, 1993, Drish *et al.* 1993).

A rotational lightcurve inversion formalism, called matrix lightcurve inversion (MLI), was previously developed by Wild (1989, 1991). This linear algebraic approach has a number of advantages over spherical harmonics decomposition. The matrix formalism readily incorporates more than one lightcurve at different aspect angles and can easily accommodate nonzero solar phase angles as well as general surface scattering and limb darkening laws. MLI can be implemented using constrained linear iterative techniques. There are many powerful mathematical tools and software packages that have been developed in the context of estimation and ill-posed inverse theory that can be exploited by MLI. Furthermore, MLI requires no a priori assumptions about the object's albedo distribution, nor does it require the surface patch areas to be dynamically changed during the iteration process for convergence. Matrix lightcurve inversion is a fundamental departure from other rotational lightcurve inversion techniques primarily because it is the first time the problem has been properly posed as a matrix equation. Consequently, the many available tools for treating well-formulated, and ill-posed, inverse problems will enable rigorous mathematical treatments (Root 1987, Tikhonov and Goncharsky 1987) to be applied to answering fundamental questions concerning the performance and limitations of lightcurve inversion (Harmon 1994).

There are three principal results arrived at in this paper. First, application of MLI to the set of Pluto rotational lightcurves (herein referred to simply as "lightcurves") over the years 1954 to 1986 indicates that they are incompatible with a static surface; this is consistent with the analysis of Stern *et al.* (1988). Second, assuming that the surface is static over the interval of 1980–1986, i.e., dynamical changes are sufficiently slow, we construct a *snapshot* image of Pluto's surface to show how it may have appeared in the 1980s. Third, the efficacy of MLI as an inversion technique is demonstrated by generating reconstructions of a highly artificial multispot model and a plausibly realistic model from their modeled noise-free and noisy lightcurves. We discuss the limitations inherent in snapshot images, the subjectively derived resolution of the images from simulations, and the future evolution of Pluto's surface.

MATHEMATICAL FOUNDATIONS

Polyhedral Surface Representation

Consider a sphere of unit radius rotating with period T inside an imaginary fixed (in space) transparent spherical surface of unit (plus some infinitesimal) radius. Further assume that each spherical surface is spanned by an identical discrete grid of latitudinal and longitudinal circles, analogous to those on any standard globe, and that the polar axes are coaligned. The internal rotating sphere will be referred to as the *object* and the outer sphere as the *template sphere*. The positive z axis corresponds to the direction of the object's angular momentum, and the x–y plane corresponds to the plane of the object's equator, and the y axis lies in the plane of the sky. We can locate points on the template sphere with standard spherical polar coordinates (θ, ϕ), where θ is the latitude coordinate and ϕ is the longitude coordinate. Then $\theta = 0$ defines the direction of the object's angular momentum, $\theta = \pi/2$ defines the plane of the object's equator, and $\phi = 0$ or $\phi = 2\pi$ for $\theta = \pi/2$ defines the positive x axis. Partition the grid into N latitude divisions and M longitude divisions of extent π/N and $2\pi/M$, respectively. Thus, the grid on each sphere consists of NM spherical rectangles or patches. The sub-Earth longitudinal meridian is defined to be at $\phi = \pi/2$.

We can reference the central latitude θ_i and central longitude ϕ_j of each patch on the grid by an ordered pair of indices (i, j), where i is the latitude index spanning the range $i = 0, 1, 2, \ldots, N - 1$, and j the longitude index spanning the range $j = 0, 1, 2, \ldots, M - 1$. Consider some arbitrary patch (i, j) and assume that it is viewed

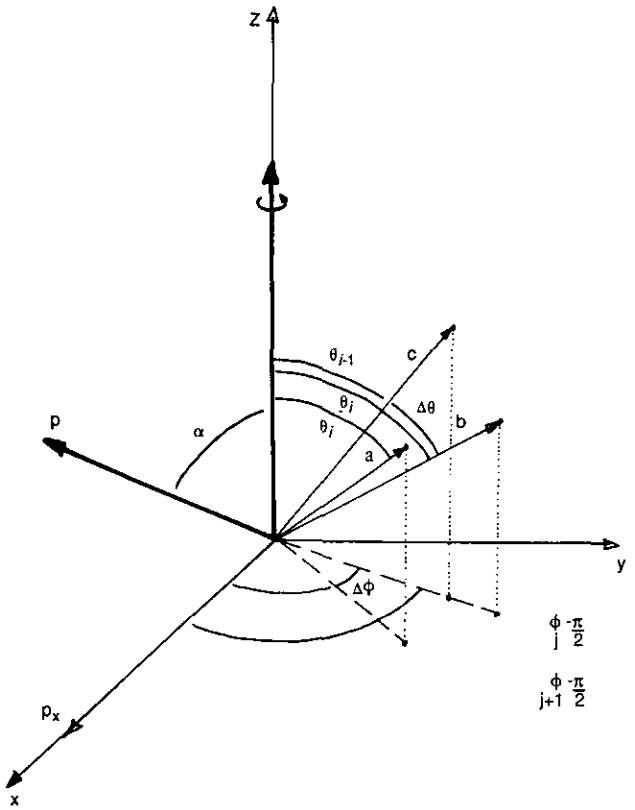

FIG. 1. The vector geometry nomenclature showing the (a, b, c) unit vectors. The d unit vector is not shown for clarity.

from the direction of the unit vector **p**. Then the projected area ξ_{ij} of patch (i, j) depends on **p** and the radial unit vectors pointing to the corners of patch (i, j) as indicated in Fig. 1. If the four unit vectors for the corners of a patch are designated as **a**, **b**, **c**, and **d**, and are indicially linked to the (i, j) patch, the projected area of the patch is given by the scalar–vector product:

$$\xi_{ij} = \frac{1}{2}\mathbf{p}\cdot(\mathbf{a}-\mathbf{c})\times(\mathbf{b}-\mathbf{d}) \tag{1a}$$

$$= \left(\frac{1}{2}\right)\begin{vmatrix} \sin\alpha & 0 & \cos\alpha \\ a_x - c_x & a_y - c_y & a_z - c_z \\ b_x - d_x & b_y - d_y & b_z - d_z \end{vmatrix}.$$

The quantity α in Eq. (1a) is the angle between the line of sight vector **p** and the axis of rotation of the body, i.e., the inclination angle, where the vector **p** is placed, without loss of generality, in the x–z plane. The north polar axis is oriented along the z axis in Fig. 1. If $\alpha = 90°$ the axis of rotation is said to be in the plane of the sky; if $\alpha > 90°$ the axis of rotation, as defined by the right-hand rule, is such that the northern pole of the object is out of view to the observer defined by **p**. The notation α is used to be consistent with that of Wild (1989, 1991) and so as not to confuse the inclination angle, i, used elsewhere in the literature with our latitudinal index i. The components of the four unit vectors in Eq. (1a) are easily determined from Fig. 1, where

$$\begin{aligned}
a_x &= \sin(\theta_{i+1})\cos(\phi_j - \pi/2)\\
a_y &= \sin(\theta_{i+1})\sin(\phi_j - \pi/2)\\
a_z &= \cos(\theta_{i+1})\\
b_x &= \sin(\theta_{i+1})\cos(\phi_{j+1} - \pi/2)\\
b_y &= \sin(\theta_{i+1})\sin(\phi_{j+1} - \pi/2)\\
b_z &= \cos(\theta_{i+1})\\
c_x &= \sin(\theta_i)\cos(\phi_{j+1} - \pi/2)\\
c_y &= \sin(\theta_i)\sin(\phi_{j+1} - \pi/2)\\
c_z &= \cos(\theta_i)\\
d_x &= \sin(\theta_i)\cos(\phi_j - \pi/2)\\
d_y &= \sin(\theta_i)\sin(\phi_j - \pi/2)\\
d_z &= \cos(\theta_i).
\end{aligned} \tag{1b}$$

With our selection of **p** to lie in the x–z plane, the angle between **p** and the z axis is the sub-Earth latitude. If the sub-Earth latitude is zero, then, as the object rotates, N patches on the object come into view (at longitude index $j = 0$ on the template sphere) and N patches move out of view for each $2\pi/M$ advance of the object. For any other sub-Earth latitude, part of the object's surface (near one of the polar regions) will remain in view for the entire rotational period, and an equal area at the opposite pole will remain out of view.

The Linear Algebraic Formulation

If the surface of the object is also divided into NM patches, we will assume that the surface albedo is constant within each patch, but that it can vary from patch to patch to form a brightness or albedo distribution over the object's surface. (We have interchangeably used the terms "brightness" and "albedo" here to describe surface behavior; the former characterizes a luminous or stellar surface, whereas the latter depicts a scattering surface. Henceforth, we use only the term "surface albedo distribution.") The lexicographic vector ordering of these NM surface patch albedo values is the *object vector* **o**. A lightcurve consisting of uniformly spaced data values is produced as the object makes one complete rotation in time period T in discrete steps in angular (longitudinal)

phase of $2\pi/M$, or steps of $1/M$ in *rotational phase* (which is normalized to the unit interval).

For the jth latitudinal band alone (M elements) the object vector is the column vector,

$$\mathbf{o}_i = \begin{bmatrix} \mathbf{o}_{i1} \\ \mathbf{o}_{i2} \\ \mathbf{o}_{i3} \\ \vdots \\ \mathbf{o}_{iM} \end{bmatrix}, \tag{2a}$$

and the object vector $\mathbf{o}$ for all NM patches is the column vector,

$$\mathbf{o} = \begin{bmatrix} \mathbf{o}_1 \\ \mathbf{o}_2 \\ \mathbf{o}_3 \\ \vdots \\ \mathbf{o}_N \end{bmatrix}. \tag{2b}$$

The object vector $\mathbf{o}$ is a fixed quantity for all aspect angles. The measured photometric lightcurves are converted into flux units, i.e., linearized, and lexicographically ordered into the *data vector* $\mathbf{d}$; note that values in $\mathbf{d}$ are dependent on the aspect viewing angle in the vector $\mathbf{p}$. The data vector $\mathbf{d}$ and the object vector $\mathbf{o}$ are related by the lightcurve matrix equation

$$\mathbf{d} = \mathbf{H}\mathbf{o} + \mathbf{n}, \tag{3}$$

where $\mathbf{H}$ is a matrix whose entries consist of the projected areas of the NM surface patches, and $\mathbf{n}$ is zero-mean signal-dependent additive noise. If a given surface patch is on the backside of the planet relative to the viewing vector $\mathbf{p}$, then the projected area computed via Eqs. (1a)–(1c) is a negative quantity. Matrix elements consisting of projected areas which are negative are set to zero in $\mathbf{H}$. The structure of $\mathbf{H}$ has an interesting feature which allows very large matrices to be readily handled and manipulated with a modest computer. As the object sphere rotates within the template sphere, the albedo of each surface patch is multiplied by a projected area element that modulated neighboring patches in the previous incremental rotational phase so that each latitudinal band consists of a square left-circulant matrix in $\mathbf{H}$ (Davis 1979, Wild 1989, 1991). For the ith latitudinal band this block matrix has the form

$$\mathbf{C}^k_{\theta_i} = \begin{bmatrix} \xi_{i1} & \xi_{i2} & \xi_{i3} & \cdots & \xi_{iM} \\ \xi_{i2} & \xi_{i3} & \xi_{i4} & \cdots & \xi_{i1} \\ \xi_{i3} & \xi_{i4} & \xi_{i5} & \cdots & \xi_{i2} \\ & & \cdots\cdots & & \\ \xi_{iM} & \xi_{i1} & \xi_{i2} & \cdots & \xi_{i(M-1)} \end{bmatrix}. \tag{4a}$$

For N latitudinal bands there are N square $M \times M$ left-circulant matrices in $\mathbf{H}$ so that for J lightcurves we can write $\mathbf{H}$ as follows (superscripts designate the lightcurve number),

$$\mathbf{H} = \begin{bmatrix} \kappa_1\mathbf{C}^1_{\theta_1} & \kappa_1\mathbf{C}^1_{\theta_2} & \kappa_1\mathbf{C}^1_{\theta_3} & \cdots & \kappa_1\mathbf{C}^1_{\theta_N} \\ \kappa_2\mathbf{C}^2_{\theta_1} & \kappa_2\mathbf{C}^2_{\theta_2} & \kappa_2\mathbf{C}^2_{\theta_3} & \cdots & \kappa_2\mathbf{C}^2_{\theta_N} \\ \kappa_3\mathbf{C}^3_{\theta_1} & \kappa_3\mathbf{C}^3_{\theta_2} & \kappa_3\mathbf{C}^3_{\theta_3} & \cdots & \kappa_3\mathbf{C}^3_{\theta_N} \\ & & \vdots & & \\ \kappa_J\mathbf{C}^J_{\theta_1} & \kappa_J\mathbf{C}^J_{\theta_2} & \kappa_J\mathbf{C}^J_{\theta_3} & \cdots & \kappa_J\mathbf{C}^J_{\theta_N} \end{bmatrix}, \tag{4b}$$

where the κ_k represents a radiometric correction so that all the data is relative to a chosen standard observer–object geometry for each lightcurve; after such a reduction is completed these radiometric factors are unity. The matrix $\mathbf{H}$ has $MJ \times MN$ elements for J lightcurves; for $J = 1$ the situation is the most ill-posed because of the highly rectangular nature of $\mathbf{H}$. If there are gaps in the rotational phase coverage then the lightcurve can either be interpolated through the gap or, preferably, all elements in the rows corresponding to the gaps in rotational phase in $\mathbf{H}$ are set to zero. In all the inversions herein the object dimension consists of $M = 40$ longitudinal and $N = 25$ latitudinal elements with $J = 1$ to $J = 5$ lightcurves used in the inversions. Because of the circulant nature of the block circulant matrices, only JMN elements of $\mathbf{H}$ need to be stored for iterative inversions. That is, a $N \times N$ circulant matrix can be fully specified by only N elements.

A generalization of MLI to accommodate arbitrary shaped objects, e.g., asteroids, has been developed by Wild (submitted for publication; see also Wild *et al.* (1994)); this formalism entails having the vector quantities $\mathbf{a}$, $\mathbf{b}$, $\mathbf{c}$, $\mathbf{d}$ being the unknowns ("vertex distances"). The circulance carries over into the definition of $\mathbf{H}$ using the template sphere concept, though the object's shape also couples into $\mathbf{H}$ so that the resulting system of equations is nonlinear (though still algebraic).

LIGHTCURVE INVERSION

Object Estimation

The process of lightcurve inversion consists of obtaining an estimate of an object's image from the object's

lightcurve(s). Using MLI an estimate of the unknowns in $\mathbf{o}$, designated as $\hat{\mathbf{o}}$, which is the reconstructed object or image (NM-dimensional vectors), is obtained given $\mathbf{d}$ (JM-dimensional vector), Eq. (3), and whatever mathematical and physical constraints are imposed on the system. That is, there are NM unknown quantities and JM linear equations constraining these quantities.

A direct inversion of the lightcurve matrix Eq. (3) is given by

$$\hat{\mathbf{o}} = \mathbf{H}^{-1}\mathbf{d}, \tag{5a}$$

However, this direct inversion is impossible, even if $J \geq N$, because the null space of $\mathbf{H}$ is nonzero whereby $\mathbf{H}$ is singular (Wild 1991). If limb darkening and nonzero solar phase angle effects are integrated into Eqs. (1) and (4) the nullity of $\mathbf{H}$ (the number of zero singular values) will diminish. For Pluto solar phase angle effects are essentially nonexistent since it never exceeds 1.9° and there is evidence that limb darkening effects may also be negligible, at least for the sub-Charon hemisphere of Pluto, since Pluto is essentially always viewed in an opposition-type geometry (Young and Binzel 1993).

More generally the generalized inverse estimate is

$$\hat{\mathbf{o}} = \mathbf{H}^{+}\mathbf{d}, \tag{5b}$$

where $\mathbf{H}^{+}$ can be practically computed as the limit

$$\mathbf{H}^{+} = \lim_{\delta \to 0} (\mathbf{H}^{T}\mathbf{H} + \delta \mathbf{I})^{-1}\mathbf{H}^{T} \tag{5c}$$

for least-squares inversion, or SVD techniques can be profitably used (Jennings and McKeown 1992). The small damping term can be replaced by a smoothing matrix to become a regularized estimator (Root 1987, Thompson and Craig 1992). Other, somewhat more esoteric, forms than Eq. (5c) for the generalized inverse exist (Campbell and Meyer 1991). In addition to the least squares inverses there are optimal estimators that use *a priori* specified first- and second-order statistics of the object, i.e., covariance matrices, to estimate the most probable object given the noisy data (Luenberger 1969); Wild (1989) discusses the use of these estimators for lightcurve inversion.

Invariably there are gaps in the data sets entailing the need for a weighting matrix $\mathbf{W}$ consisting of unity and zero diagonal entries to operate on $\mathbf{H}$. The zero entries in $\mathbf{W}$ act to zero out those rows of $\mathbf{H}$ corresponding to longitudes where there are gaps in the rotational phase. In a more rigorous treatment the elements of $\mathbf{W}$ are proportional to the photometric flux signal, i.e., $\mathbf{W}_{ii}^{-1/2} = 1/\sigma_i$ where σ_i^2 is the variance of the ith data point, for each rotational phase increment whereby Eq. (3) is operated upon by $\mathbf{W}^{-1/2}$ on all terms to derive the weighted (or damped) least squares inverse estimator (often called the Gauss–Markov estimator). In our analysis we set to zero the elements in those rows of $\mathbf{H}$ that correspond to points in the rotational phase where there are gaps.

Equation (5b) can be implemented using SVD techniques, which in fact are a form of smoothing when small singular values are set to zero so that components of the noise vector that would otherwise be amplified by these small singular values are put into the null space of $\mathbf{H}$. That is, the solution is smoothed in the sense that the troublesome noise components are filtered out so that they are not inverted. In the case where the kernel is singular, the SVD method finds the solution which minimizes the least-squares residual subject to the constraint that the solution vector has the smallest Euclidean norm. (In other words, the sum of the squares of the components of the solution vector should be minimized. For the MLI case, this corresponds to minimizing the sum of the squares of the albedos of all the surface elements.) Hence, SVD can be viewed as a regularized solution in which the smoothing constraint is that the solution has the minimum Euclidean norm out of all solutions which have the smallest possible residual. However, there is no reason to think that Pluto's surface features should try to minimize the sum of the squares of the albedos of the patches! The bias toward minimum Euclidean norm of the solution means that solutions consisting of bright spots on a dark background will be preferred to solutions consisting of dark spots on a bright background (Harmon 1994).

We estimate the object vector $\mathbf{o}$ using an iterative regularization technique. Using regularization allows a variety of smoothing constraints to be evaluated and the most successful to be selected; examples include first and second derivative smoothing and maximum entropy. With SVD there is no explicit smoothing constraint, thus removing some freedom in generating reconstructions. After each iteration albedo boundedness in [0, 1] can be implemented. The constrained iterative regularization methods are inherently nonlinear; this makes it difficult to quantitatively determine the error propagator for the system. The error propagator is the ratio of variance in the reconstruction to the variance in the data due to noise, and sometimes referred to as the noise gain. The error propagator is handily found using purely linear SVD techniques or unconstrained iterative methods. Furthermore, large object dimensions imply uncomfortably large $\mathbf{H}$ matrices and iterative techniques can take advantage of the cyclic nature of $\mathbf{H}$ to minimize storage requirements. Also, speed enhancements can be made because operation on a vector by a left-circulant matrix corresponds to cross-correlation of the first row of the matrix with the vector; this means that the multiplication can be sped up by performing the computations using fast Fourier

transforms. For the present work we did not take advantage of this speed enhancement.

The constrained Jacobi iteration can be used to estimate $\mathbf{o}$, where $\hat{\mathbf{o}}^{(n)}$ is the nth iterate of the object estimate (Press *et al.* 1986, Spedicato 1991):

$$\hat{\mathbf{o}}^{(n+1)} = \hat{\mathbf{o}}^{(n)} + \beta \mathbf{H}^T(\mathbf{d} - \mathbf{H}\hat{\mathbf{o}}^{(n)}) - \lambda \mathbf{S}\hat{\mathbf{o}}^{(n)}, \quad \hat{\mathbf{o}}^{(n)} \in [0,1]. \tag{6a}$$

β is an acceleration parameter, λ is a smoothing parameter ideally chosen so that the reconstruction does not exceed the noise level in the data, and $\mathbf{S}$ is a Laplacian smoothing matrix (Twomey 1963, 1977). Young and Mai (1991) and Press *et al.* (1986) discuss the optimal choice of β as well as more efficient iterative estimators than the Jacobi technique used here. For inversions with $J \leq 3$ we use $\beta = 2$, and for $J \geq 4$ we use $\beta = 1$; these choices ensured uniform convergence in the root mean squared (rms) lightcurve error (see below, Eq. (7)). We choose $\hat{\mathbf{o}}^{(0)}$ to be a constant for all surface elements (0.6), though an equally good initial estimate is $\hat{\mathbf{o}}^{(0)} = \mathbf{H}^T\mathbf{d}$. The Jacobi implementation in Eq. (6a) converges notoriously slowly, though this was not a concern nor difficulty for arriving at our results. Vastly superior convergence speed with MLI can be attained by using the conjugate gradient minimization algorithm with typically on the order of 30–100 iterations which can be accomplished in minutes on an IBM RS/6000 workstation (Harmon 1994).

For each nth-object estimate $\hat{\mathbf{o}}^{(n)}$ the lightcurve error vector is

$$\mathbf{e}^{(n)} \equiv \mathbf{d} - \hat{\mathbf{d}}^{(n)} = \mathbf{d} - \mathbf{H}\hat{\mathbf{o}}^{(n)}. \tag{6b}$$

The imposition of a [0,1] albedo boundedness constraint upon performing each iteration in Eq. (6a) is, interestingly, very powerful in regard to narrowing the acceptable class of solutions of $\mathbf{o}$ in Eq. (3) by filtering out those components of noise in the solution that are inconsistent with this constraint (Lucy 1992). Nonnegativity is of critical importance in ill-posed problems not too dissimilar to the present paradigm (cf. Gindi *et al.* 1984, Smith *et al.* 1985).

The figure of merit used to describe performance of MLI is the rms *lightcurve error* ε. It is computed from all JM entries in $\mathbf{e}^{(n)}$ using the formula

$$\varepsilon = \sqrt{\frac{1}{JM}\sum_{k=1}^{J}\left[\sum_{j=1}^{M}(e_k^{(j)})^2\right]}, \tag{7}$$

which is convertible to the χ^2 statistic with equal (unity) weighting for elements of $\mathbf{d}$ (via $\mathbf{W}^{-1/2}$) in Eq. (6b). The rms lightcurve error ε initially decreases exponentially with each iteration and then slowly converges to an asymptotic value, which depends on the noise in the data and choice of smoothing constant, and where the $e_k^{(j)}$ are the elements of the lightcurve error vector in Eq. (6b) for the kth lightcurve. The true rms object error is unknown in practice.

In the absence of smoothing the solution for $\mathbf{o}$ from Eq. (3) is nonunique because there may be an infinite number of solutions that will have the same χ^2 statistic. When smoothing is included, the smoothest solution out of all those with the specified χ^2 is singled out and selected as "the" solution. That is, when smoothing is included the nonuniqueness disappears. Furthermore, the use of smoothing will, for the most part, alleviate the need for the albedo positivity constraint, i.e., the albedo constraint is not responsible for the convergence of the solution. The gross features of the solution remain intact for a wide range of smoothing parameter values. As the smoothing parameter is decreased (less smoothing) the albedo map shows increasing resolution manifested as sharper edges and closely spaced spots become separately resolved, etc. However, the same bright and dark regions appear in the image independent of the smoothing parameter's value. There is a limit to this process since if too little smoothing is used noise artifacts begin to dominate the reconstruction, rendering it useless.

Harmon (1995) has examined in detail the question of attainable surface resolution of the MLI technique given a specific set of lightcurves, noise in the data, the latitude dependence, etc. Some qualitative observations are given in Wild *et al.* (1994) for the single lightcurve case, and we discuss this issue further below.

Determining the Optimal Smoothing Parameter

The optimum value of the smoothing constant λ depends on the amount of noise in the data. Ill-posed problems are prone to instabilities because of noise in the data and smoothing constraints stabilize the solution (Turchin *et al.* 1971). Different strategies exist for choosing the smoothing parameter λ. The first is to empirically estimate the optimal smoothing parameter λ by conducting simulations with noise, using the measured data, and estimating the approximate value such that discernible noise-induced artifacts do not appear. A second more quantitative approach is to examine the variance of the lightcurve discrepancy, i.e., $\mathbf{d} - \hat{\mathbf{d}}$, where $\hat{\mathbf{d}}$ is the lightcurve of the reconstructed object, and to find the smoothing parameter such that this variance is consistent with the known noise level in the data. Thompson and Craig (1992 and references therein) discuss various other approaches for the choice of the smoothing parameter in the context of astrophysical inverse problems.

To understand the effect of noise in the reconstruction,

TABLE I
Lightcurve Data Sets

Year	N_p	Sub-Earth Lat. (deg)	Observer(s)	Notes
1986-90	43	-3.0 to 5.0 α=93° to α=85°	Kiladze, Kukhianidze	Exceptionally noisy data (estimated ±0.1 error bars in the B,V magnitude data)
1986	44	-3.0 α=93°	Tholen, Buie Lark	Very high quality data; considered the "standard"
1982	31	-11.0 α=101°	Binzel, Mulholland	Extraneous "hump" feature near 0.3 rotational phase
1981	18	-13.4 α=103.4°	Tholen, Tedesco	Shape similar to 1986; large gaps in rotational phase coverage
1980	24	-15.5 α=105.5°	Tholen, Tedesco	Consistent with 1981; can be merged with 1981 dataset
1975	12	-25.9 α=115.9°	Lane, Neff, Fix	Excessively noisy; poorly sampled over rotational phase
1973	28	-29.5 α=119.5°	Neff, Lane, Fix	Noisy; "bunched" in rotational phase domain
1972	18	-30.5 α=120.5°	Andersson and Fix	Very noisy
1964	14	-44.6 α=134.6°	Hardie	Moderately noisy; poor rotational phase sampling
1954	21	-54.6 α=144.6°	Walker, Hardie	Moderately noisy; Kuiper's six 1953 points excluded

we may construct a lightcurve that is a constant value over all rotational phases but with a solitary point having a value above this level. A reconstruction is generated from this lightcurve. The [0, 1] constrained iterative inversion will produce a reconstruction whose lightcurve is a gaussian-centered noise spike (though with a smaller peak amplitude). The reconstruction is a wedge-type feature bounded between longitudinal meridians where the longitudinal width is a function of the noise spike amplitude. Reconstructing noisy data with a smoothing parameter that is too small results in these wedges forming. Further, cusps in the data, i.e., first-derivative discontinuities, create cross-meridianal features in the map. The latter artifact appeared when, very early on in our application of MLI to Pluto's lightcurves, we *a priori* smoothed the data without properly accounting for the cyclic nature (periodicity) of the lightcurves at the endpoints of the rotational phase.

ROTATIONAL LIGHTCURVE REDUCTIONS

The Lightcurve Data Sets

The lightcurve data sets are summarized in Table I; they are discussed in detail in Mercialis (1988). Each data set consists of pairs of numbers $(t, m(t))$, where t is the time of the measurement and $m(t)$ is the measured visual (V) magnitude of Pluto (and Charon). These data, with the addition of the more recent 1986 lightcurve (Buie and Tholen 1989), are identical to that used in Marcialis (1988); all have been reduced to a common viewing geometry with mean opposition and heliocentric distance of 39.5 AU, geocentric distance of 38.5 AU, and solar phase angle of 1°. The data have also been corrected for light travel time. The $(B-V) = +0.82$ color index is used to convert B to V magnitudes to compare with data acquired before 1980. This choice of $B-V$ is adopted because the photometry is integrated over the whole Pluto–Charon system. There is evidence that Pluto's color varies as a function of rotational phase (Tholen and Tedesco 1984; Marcialis and Lebofsky 1991). Our choice of this $B-V$ value assumes that Charon has only a small, if any, lightcurve of its own and that its color is relatively independent of longitude; consequently, a representative $B-V$ for the system can be chosen. Since the color does not vary by more than 1 or 2% throughout a rotation, this is a good approximation. It should be pointed out that Pluto's $B-V$ may not have remained constant over the 30-year interval spanned by the photometry. The sub-Earth latitude has changed and there may also be seasonal effects; there is

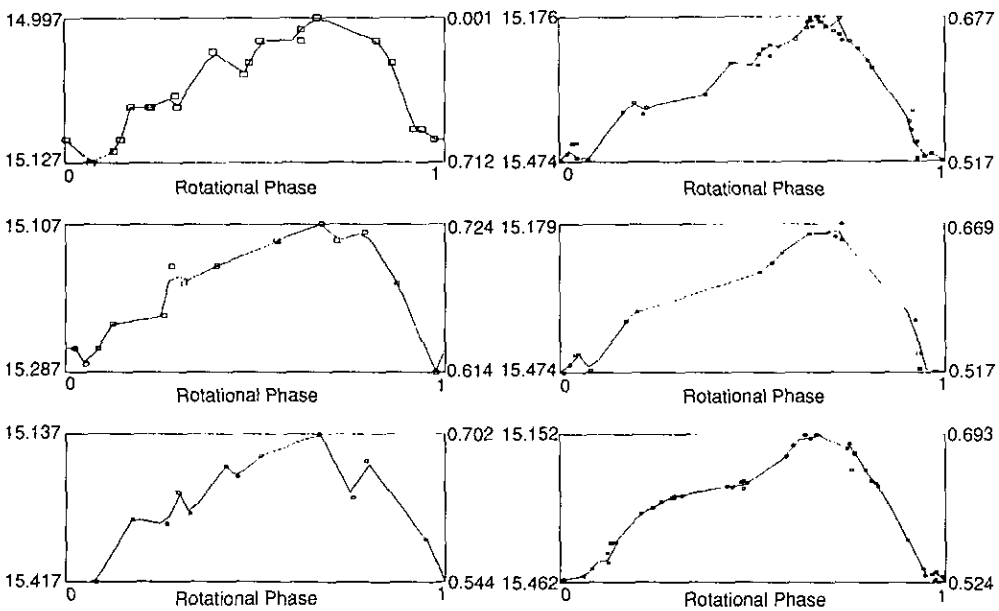

FIG. 2a. (Top left) The 1954 lightcurve; (center left) the 1964 lightcurve; (bottom left) the 1975 lightcurve; (top right) the merged 1980 and 1981 lightcurve; (center right) the 1981 lightcurve; (bottom right) the 1986 lightcurve. A running median trace goes through the lightcurves. These data are all shown in V magnitude and a 0.167 correction is added to all data to remove the contribution from Charon. These data are plotted directly from the tabulated data shown graphically in Marcialis (1988). All images in this article have been produced from these data after suitable reductions have been carried out.

no known way to go back and account for any variation. [Binzel (1988) determined (B–V) for the anti-Charon hemisphere of Pluto to be 0.867 ± 0.008 and the sub-Pluto hemisphere of Charon to have $(B-V) = 0.700 \pm 0.010$ from mutual event multicolor photometry; from this Charon $(B-V)$ color index Binzel (1988) notes that this is nearly the same as the incident sunlight $(B-V) = 0.65$ value, implying that Charon is a gray, or neutral colored, object.]

We follow the prescription presented by Marcialis (1988) in our usage of the lightcurves presented in Table I. Kuiper's six points obtained in 1953 are excluded and Kiladze's (1967) data is not used. Kuiper's six points clearly increase the noise variance when used with the data of Walker and Hardie (1955); this implies that these data are not properly calibrated (Marcialis 1988). The data acquired in the 1970s by Lane *et al.* (1976), Neff *et al.* (1974), and Andersson and Fix (1973) are very noisy. The 1973 lightcurve is confined within the upper half of the rotational phase domain. The 1980, 1981, and 1982 lightcurves can all be merged together, though the 1982 lightcurve (Binzel and Mulholland 1984) has a spurious bump at 0.3 rotational phase that is counter to the general trend exhibited (the "shelf" feature) by other lightcurves taken concurrently. Burwitz *et al.* (1991) merge lightcurves over the years 1982–1990 and assume an axis in the plane of the sky for their 1D longitudinal deconvolution of the rotational lightcurves. Buie and Tholen (1989) published a lightcurve acquired in 1986, which we reduced for our analysis to the common viewing geometry. This lightcurve appears to be the most complete in regard to rotational phase coverage and clearly is the least noisy of the ensemble of lightcurve data available at this writing. We use this lightcurve as the reference standard from which we judge the quality of the other data sets in Table I. An additional data set was recently published by Kiladze and Kukhianidze (1992), but the data are exceptionally noisy and unusable for our analyses. The original lightcurve data used in our inversions are plotted in Fig. 2a. It should be noted that these plots may appear to deviate slightly from those of Marcialis (1988); this is simply because Marcialis (1988) hand drew the data and our plots are computer drawn from the tabulated data.

Reductions for Use with MLI

The reductions for the 1986 lightcurve (Buie and Tholen 1989) proceed as follows. Assuming a phase coefficient of 0.037 mag/deg, and correcting the published tabulated lightcurve to mean opposition using $r = 39.5$ AU heliocentric distance, $\Delta = 38.5$ AU Earth–Pluto distance, and $\alpha_S = 1°$ the solar phase angle, via the formulae,

$$t_{\text{corr}} = t_{\text{obs}} - \left[\frac{0.005775518 \text{ days}}{\text{AU}}\right][\Delta \text{ AU}], \qquad (8a)$$

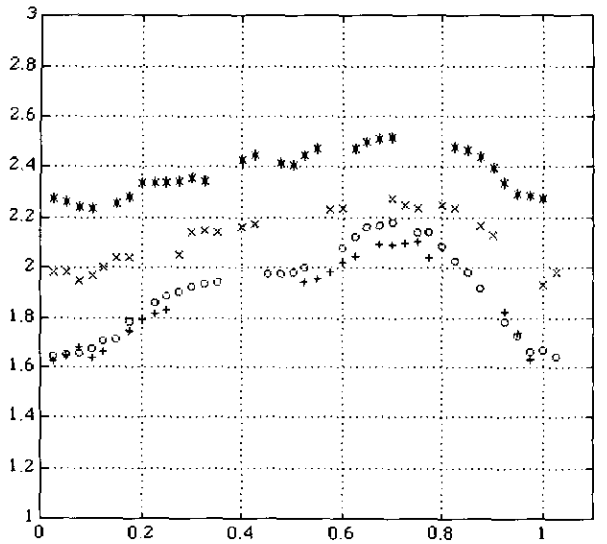

FIG. 2b. The normalized disk-integrated lightcurves for 1954 (*), 1964 (x), 1981 (+), and 1986 (o). These data are used directly by MLI and are normalized to the interval [0, π]. Regions in rotational phase where there are gaps have corresponding rows in the H matrix set to zero.

and

$$B_{\text{corr}} = B - 5\log_{10}\left\{\frac{r\Delta}{(39.5)(38.5)}\right\} - 0.037\{|\alpha_s| - 1^\circ\}. \tag{8b}$$

Here Eq. (8a) is the light travel time correction for the Julian date of the observation and Eq. (8b) is the B magnitude at the standard viewing geometry adopted for Pluto (Marcialis 1988), and $|\alpha_s|$ is absolute magnitude of the solar phase angle at the time of observation. The results of applying Eqs. (8a) and (8b) to the 1986 lightcurve are given in Table II.

Pluto may be regarded to be a sphere viewed at an opposition geometry at all times so each magnitude measurement represents the integrated brightness of Pluto over a projected area of π (assuming that the radius is normalized to unity). Without limb darkening $\Sigma_{i,j}\xi_{ij} = \pi$, incorporating limb darkening in the definition of ξ_{ij}, gives an effective total projected area of $\Sigma_{i,j}\xi_{ij} < \pi$. Herein we assume that Pluto exhibits no limb darkening effects. Young and Binzel (1993), and Young (1992), give evidence for this assertion wherein they estimate Pluto's global normal reflectance from the observed sub-Charon geometric albedo. They show that the Minnaert limb darkening coefficient is close to 0.5, indicating no substantial limb darkening. However, Young and Binzel (1993) emphasize that a more careful analysis is needed utilizing inferior and superior mutual event lightcurves to properly separate out the correlated effects of Pluto's radius and limb coefficient.

Each Pluto lightcurve data set is assumed to be viewed from the sub-Earth latitude indicated in Table I. Further, we assume that the contribution of Charon to the V magnitude data for Pluto merely alters the relative brightness of the surface elements, so that the absolute locations of surface features are unaffected by the contribution of Charon to the V magnitude. That is, we assume that Charon has no intrinsic lightcurve at visual wavelengths to contaminate Pluto's lightcurves. To correct for Charon, we subtract a constant value of 0.167 magnitude from each measured visual magnitude $m(t)$ (cf. Olkin *et al.* 1993, Buie and Shriver 1994). The assumption of Charon as a featureless sphere is corroborated by recent observations of the individual lightcurves of Pluto and Charon (Olkin *et al.* 1993) where B filter lightcurves of Charon are stated to be consistent with zero peak-to-peak amplitude variation.

The inversion formalism requires the "alignment," or phase shift, of all lightcurves for the same object, i.e., the zero rotational phase point in each lightcurve is referenced to a sub-Earth longitude meridian that is fixed on the planet. The time t for each measurement is transformed to the rotational phase domain p by the modulus of the time with respect to the synodic rotational period of Pluto, $T = 6.3872$ days,

$$p = \text{mod}(t - J_d, T), \tag{9}$$

where J_d is the reference Julian day. After this transformation, each data set consists of pairs of numbers (pT, $m(pT)$), where p is the rotational phase of the measurement and $m(pT) = m(t)$ is the measured visual magnitude of Pluto.

In general, the number of points in each lightcurve data set will not correspond to the choice of M and the data will be unequally spaced in rotational phase. Only those rotational phase points which have nearest neighbor data points are used; the gaps are weighted to zero in the **H** matrix. Linear interpolation is used on the nearest neighbor data points to obtain those points that have a spacing of duration $2\pi T/M$. Each data set then consists of at most M points $m_j = m_j(pT)$, where m_j is the V magnitude for longitude index j. We investigated the feasibility of interpolating the data across regions where there were substantial gaps in the rotational phase coverage, but this causes two difficulties. The first is that an interpolation usually follows some simple power law but, particularly for large gaps, the true (unmeasured) lightcurve may be significantly different. This will adversely affect the reconstruc-

TABLE II
Buie and Tholen (1989) 1986 Lightcurve Data Reduced to Common Viewing Geometry

Jd at mean opposition	B magnitude	(stn dev)
2446413.96885	15.9595	0.0028
2446427.95387	15.9244	0.0045
2446428.96096	15.8280	0.0075
2446432.95749	15.9682	0.0023
2446441.93542	15.8271	0.0023
2446442.90659	15.9287	0.0028
2446442.95220	15.9352	0.0032
2446443.87832	16.1330	0.0034
2446443.93767	16.1368	0.0033
2446444.88124	16.0544	0.0046
2446444.97135	16.0533	0.0043
2446445.94620	15.9584	0.0009
2446448.88501	15.9008	0.0122
2446495.94474	16.0957	0.0185
2446497.93416	15.9347	0.0051
2446498.91059	15.8722	0.0058
2446499.90975	15.8559	0.0070
2446500.90515	16.0476	0.0062
2446501.92245	16.1238	0.0066
2446502.88631	15.9912	0.0053
2446509.81724	15.9605	0.0012
2446509.94949	15.9551	0.0019
2446513.93863	16.1084	0.0032
2446523.74753	15.9401	0.0062
2446539.70382	16.1162	0.0028
2446539.81192	16.1257	0.0045
2446539.93001	16.1326	0.0020
2446540.70530	16.0540	0.0057
2446541.76522	15.9557	0.0012
2446542.72636	15.9357	0.0030
2446542.87207	15.9274	0.0030
2446543.73120	15.8504	0.0047
2446544.65583	15.8457	0.0079
2446544.74978	15.8651	0.0030
2446577.84515	16.1228	0.0090
2446578.72366	16.1093	0.0053
2446579.73272	15.9804	0.0040
2446589.74267	15.9230	0.0041
2446590.73404	16.1186	0.0048
2446591.73645	16.0748	0.0045
2446608.61489	15.8673	0.0014
2446608.80316	15.9007	0.0031
2446619.63145	15.9280	0.0021
2446620.68167	15.8370	0.0019

tions. Second, interpolation tends to produce cusps which will lead to undesirable artifacts in the image.

Each Pluto lightcurve consists of V magnitudes and these must be converted to flux units for the data vector **d** in the linear MLI technique. The V magnitude data m_j is converted to the d_j in **d** using the magnitude-flux equation

$$d_j = \pi 10^{0.4(m_o - m_j)}, \tag{10}$$

where m_o is a reference magnitude, such as that of the Sun. The π factor in Eq. (10) arises because entries in **d** are normalized to the interval $[0, \pi]$.

MLI is the matrix equivalent form for the inversion of the Fredholm integral equation of the first kind that is implicit in Eq. (10) (Wild 1989), i.e.,

$$10^{0.4[m_s - m(p)]} = \frac{\kappa}{\pi} \int_S \xi(\theta, \phi - 2p\pi) A(\theta, \phi), \tag{11}$$

where m_s is the magnitude of the sun, κ is a radiometric factor, ξ the projected area of a small surface patch centered on the specified coordinates with p being the rotational phase, and $A(\theta, \phi)$ is the geometric scattering albedo at a point on the planet's surface. The ϕ-$2p\pi$ dependence in the ξ kernel reflects the transformation from template sphere coordinates to body-fixed coordinates, where θ and ϕ are defined to be body-fixed coordinates in Eq. (11), and shows that this is a linear shift-invariant process, i.e., a convolution kernel. If the scattering properties of Pluto's surface are known or assumed a priori then with $m_o = m_s$ the Sun furnishes an absolute flux standard and the only remaining free parameters are attributes of the surface physics. We assume uniformly geometric scattering over the entire surface, which is considered to be a reasonable assumption for asteroid regoliths at zero solar phase angle (French and Veverka 1983). Pluto is effectively always in an opposition geometry though the validity of this assumption depends on the scattering physics of the various surface ices. The choice of m_o will affect the absolute geometric albedo of surface features, though not their relative albedos, position, shape, etc. We adopt $m_o = 14.757$ based on the assumption that for the point in the rotational phase corresponding to the brightest point in the 1954 lightcurve Pluto has an average surface albedo of 0.8 (normalized to disk-integrated brightness this is 2.513). This value for m_o is used in the conversion of all the lightcurves to entries in **d**. Figure 2b shows the 1954, 1964, 1981, and 1986 lightcurve data, after conducting the necessary conversions, which are in **d**.

Since Charon was discovered the pole orientation of Pluto has been determined with high accuracy and therefore the aspect angle is well characterized for all lightcurves. Consequently, the aspect angle is introduced as an *a priori* known quantity into our inversions.

QUALITATIVE INFERENCES

Stern *et al.* (1988, Fig. 1; see also Buie and Tholen 1989, Fig. 2) show the smoothed 1954, 1964, 1975, and 1982 lightcurves in V magnitudes on the same graph. These data readily show the secular decline in average brightness, the increasing in lightcurve amplitude from

1954 to 1982, and the formation of the "shelf" feature centered around rotational phase 0.3 (Buie and Tholen 1989). The 1986 lightcurve, not shown in those plots, is slightly brighter than the 1982 lightcurve; the brightening trend is illustrated in Buie and Tholen (1989, Fig. 3). In 1954 Pluto's aspect was with the southern polar region in full view; i.e., the sub-Earth latitude is $-54°$ (see Table I). In 1986 the axis of rotation is nearly in the plane of the sky and the south pole is tilted 3° toward us. In this section we give a qualitative assessment of the consistency of these lightcurves assuming a static surface by examining their averages, amplitudes, and changes in the lightcurve between 1954 and 1986. In all our analyses we assume that the lightcurves are caused strictly by surface albedo variations.

Using Lightcurves Closely Spaced in Aspect Angle

A serious concern when we generate images from lightcurves closely spaced in time is the small change in Pluto's aspect angle. From 1981 to 1986 it has changed by ~10°. Is this sufficient to discern latitudinal surface variations over the entire surface or just part of the surface? The answer, as determined from numerous simulations, appears to be dependent on the noise variance relative to the change in mean lightcurve level between the two lightcurves and the structure of the surface features involved.

Consider presently an object with a complicated overall albedo map but with an extended and uniformly bright axis-centered polar cap. A single lightcurve cannot reconstruct the polar cap without a priori information about its existence because the polar cap does not contribute to photometric modulation in the rotational lightcurve. If two noise-free lightcurves L_1 and L_2 could be acquired at slightly different aspect angles, i.e., one with $\alpha_1 = \alpha(t_1)$ and the other with $\alpha_2 = \alpha(t_2)$ with $t_2 = t_1 + \Delta t$ and $\alpha_1 > \alpha_2$ (analogous to Pluto's behavior with our aspect angle nomenclature, given in Fig. 1), and the mean values are such that $\bar{L}_1 < \bar{L}_2$, a bright region situated in proximity to the northern axis will appear in the reconstruction from these two lightcurves. With the inclusion of noise the error in the estimate of the difference in the lightcurve means, i.e., $\bar{L}_2 - \bar{L}_1$, will increase as the variance of the noise in L_1 and L_2, with the result that the size, longitudinal extent, and even proper axis of location of the polar brightening will change. If the noise variance in the lightcurves is sufficiently large no bright polar region may appear. The analogy can be extended to general axially symmetric features such as bands because such features contribute only to the mean level between lightcurves measured at different aspect angles. If the difference in aspect angles between lightcurve measurements is large then a correspondingly larger measurement noise variance is needed to mask out the presence of the axially symmetric feature. In other words, the reconstruction of axially symmetric features, particularly for snapshot images—those defined to be taken from two or more lightcurves with aspect angle changes that are small, i.e., ~10°—are extremely sensitive to noise in the data.

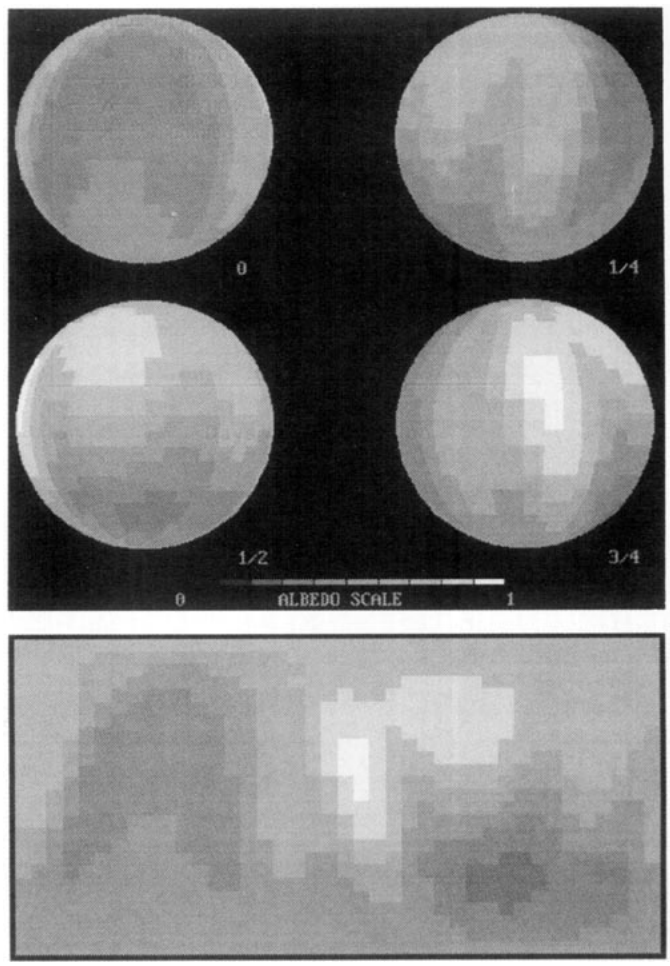

FIG. 3a. (Top) First Pluto snapshot image. Spherical representation surface map using the 1981 and 1986 lightcurves. The sub-Charon hemisphere in our maps corresponds to the 1/4 rotational view of the planet. North is up in all of these figures. (Bottom) Mercator map representation.

An inspection of the combined lightcurve plot in Stern *et al.* (1988, Fig. 1) very rapidly convinces one that under the assumption of a static surface that something very bright was persistently pointing toward us, over all rotational phases, in 1954 and receded away as the years passed and as Pluto's aspect angle migrated to its present state. Such a persistent feature must be a bright region in the proximity of the south pole. Because of measurement noise, with only a small change in aspect between two

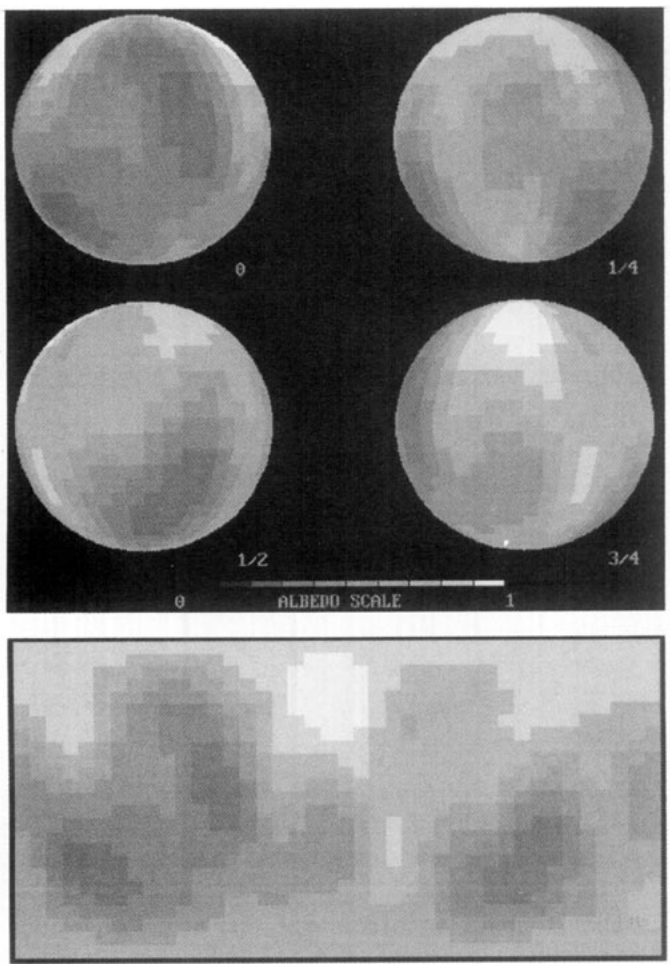

FIG. 3b. (Top) Second Pluto snapshot image. Spherical representation surface map using the merged 1980 and 1981 lightcurves in conjunction with the 1986 lightcurve. (Bottom) Mercator map representation.

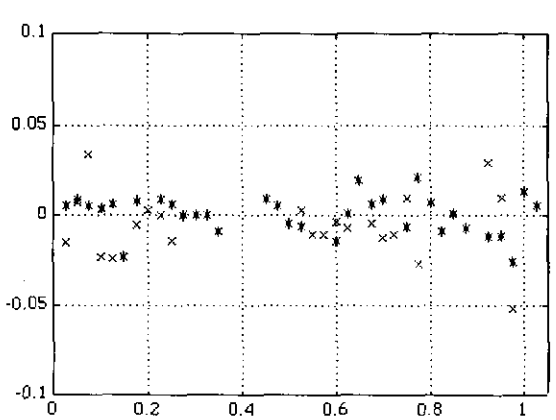

FIG. 3c. Residuals between the lightcurve fit obtained by using MLI and the 1981 and 1986 lightcurve data sets that were used in the reconstruction of Fig. 3c. Here * is the 1986 residual data and x is the 1981 residual data.

lightcurves it is essential that the noise variance be significantly less than the average change in mean lightcurve level. Therefore, to construct useful snapshot images of Pluto using lightcurves taken only a few years apart it is necessary to absolutely minimize sources of error and noise.

Consistency of the Pluto Lightcurves

Referring to the illustration of Stern *et al.* (1988, Fig. 1), Pluto has dimmed about 0.3 V magnitude between 1954 and 1982. After 1982 Pluto brightened somewhat, suggesting that a bright region is in view over all rotational phases. However, the aspect angle difference is about 12°; is this change commensurate with the average brightness increase? Only a very small polar region, particularly in regards to projected area, surrounding the north pole has come into view. Further, can the 43° change in aspect satisfactorily account for the mean change of 0.3 magnitude from 1954 to 1982? MLI will generate an image that fits the furnished data and constraints by minimizing Eq. (7). Assuming photometric consistency and that the surface is truly static MLI should produce an image that fits all the lightcurves in the 1954–1986 interval to within the noise level in the data. Noise artifacts should appear in the images when the lightcurve fits get below the noise level provided that the iterations do not converge prior to reaching this level. That is, if the data are inconsistent because the surface is not static, MLI will converge to an image before the noise level is reached. Conversely, if the MLI reconstruction converges toward an image prior to reaching the noise level (and the associate noise-induced artifacts do not appear) then we may conclude that the lightcurves are consistent with a nonstatic surface.

Pluto's mean lightcurve magnitude has changed from 1954 to 1982 and is ~0.3 magnitude (~30%) and Pluto's aspect changed from having all areas greater than 54° south latitude in full view to having polar regions to being approximately 50% in view. Therefore, half of the total projected area of this polar feature accounts for Pluto brightening by 0.3 magnitude. Assume the presence of a large southern polar cap. A high albedo (~1) polar cap that extends from the equator to the pole covers in excess of 80% of Pluto's projected area in 1954, and covers somewhat more than 50% in 1982, which is consistent with a 30% change in mean lightcurve brightness. If Pluto's surface is static over this interval, then the region of the surface that causes the ~0.1-magnitude 1954 lightcurve variation is constrained to lie at northern latitudes between 0° (the equator) and +36°. The additional ~0.2-magnitude variation in the 1982 (or 1980 and 1981) lightcurve must be caused by features above a north lati-

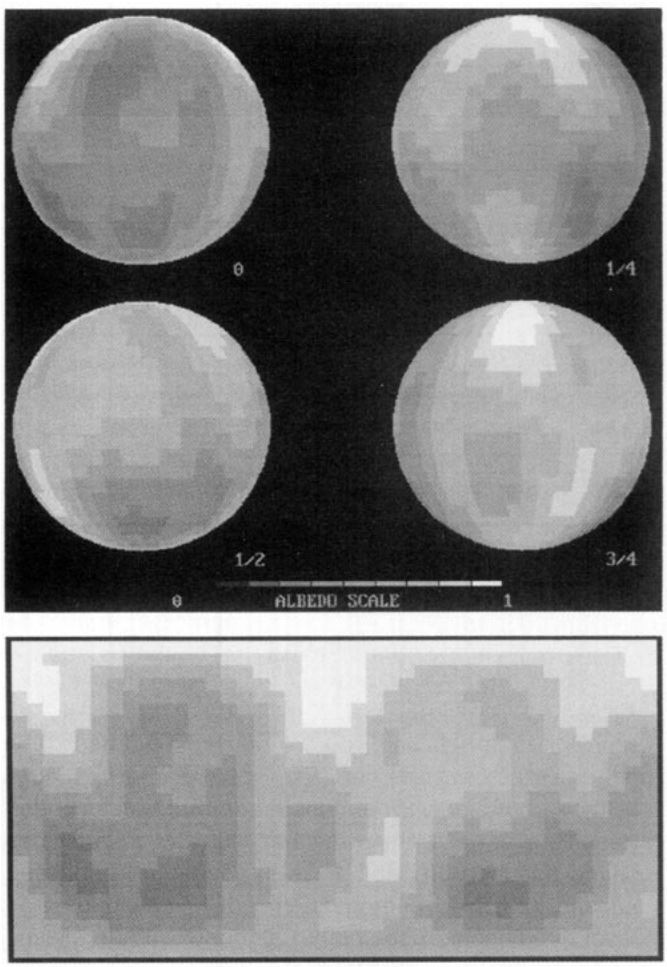

FIG. 3d. (Top) Third Pluto snapshot image. Spherical representation surface map using the 1980 and 1986 lightcurves. (Bottom) Mercator map representation. Some brightening in the south polar region region appears in this map.

tude of 36°, though the northern polar region must be dark otherwise the mean change in lightcurve level cannot be caused by our hypothesized full southern bright polar cap moving out of view. If the northern regions above 36° latitude are bright then the southern polar area would have to be larger, implying that the near-equatorial latitude band where the 1954 lightcurve variations exist would get even narrower, i.e., confined to latitudes below 36°, and with greater albedo contrast or excursions from that of the bright southern region. Now let us include the 1986 lightcurve in our thought experiment. Whatever lies above the northern 36° latitude meridian cannot be mostly dark but contribute about a factor of three to the lightcurve amplitude as compared to1954, as deduced from an examination of the Stern *et al.* (1988) Fig. 1 or the Buie and Tholen (1989) Fig. 2. The change in the orbital lightcurve at the "max" point in the lightcurve is approximately 0.15, whereas it is approximately 0.3 magnitude for the "min" portion of the lightcurve, so bright areas must exist above north latitude 36°. However, when 1986 is included, it demands that a further fraction of the bright southern region has moved from view (now at almost exactly 50%) and that a small bright northern polar area has entered into view in addition to whatever bright regions existed to explain the large 1982 lightcurve amplitude variation; this is required to account for the overall brightening of the 1986 lightcurve. The entire bright area must be constrained to lie about north latitude 78°, which is feasible with 1986 being about 0.02 magnitude brighter than 1982 on average. Therefore, the presence of the small bright cap for the 1986 lightcurve plus the bright regions to satisfy the increased 1982 lightcurve amplitude variations have the effect of increasing the high albedo southern polar cap to go into northern latitudes and hence to compress the region over which lightcurve amplitude variations may occur for 1954 and hence also subsequent lightcurves. Further, with the latitude band for variations made smaller the albedo contrast variations increase toward the maximum allowed in [0,1], i.e., very dark and very bright only or from close to zero albedo to near unity albedo. The conclusion to be drawn from this exercise is that the ensemble of lightcurves from 1954 to 1986 are not mutually consistent with each other and hence MLI should demonstrate this effect by being unable to fit all the lightcurves selected from any grouping of lightcurves that uses one or both members of the set {1954, 1964} with one or more members of the set {1980, 1981, 1982} and with {1986}. Further, MLI should fashion an image with a large bright southern polar cap, a narrow high contrast band above this southern polar region, and a bright, possibly irregular, northern region. Consequently, the constrained inversion will be unable to simultaneously fit these lightcurves to within the noise level in the data.

INVERSION OF PLUTO LIGHTCURVES

Snapshot Images from the 1980s Lightcurves

The MLI method was first applied to the 1980s Pluto lightcurves. The value for λ, empirically determined such that no obvious noise artifacts appeared, is $\lambda = 0.0005$ for all Pluto reconstructions. This value of λ is not optimal, but is close to optimal. Iterations continue until the rms lightcurve error ε, Eq. (7), remains constant in the fourth decimal place over at least 10,000 iterations. Both spherical and Mercator MLI maps of Pluto using the 1981 and 1986 lightcurves are shown in Fig. 3a. The rms lightcurve error using Eq. (7) converged to 0.0116. Pluto is shown

at 0.25 rotational increments in the spherical rendition; for the 1/4 rotation view the sub-Charon point lies on the central meridian of the image and this meridian lies at zero rotational phase on the Mercator projection maps (the left edge). A complete rotation or 6.3872 days brings us back to the top left of Fig. 3a; the bottom map in Fig. 3a is the equivalent Mercator projection map. The pixel scale is ~145 km in latitude by ~180 km in longitude or 7 by 8 mas at 30 AU. Figure 3b depicts the reconstruction where the 1980 and 1981 lightcurves are merged to reduce gaps in rotational phase with an aspect angle of $\alpha = 104.5°$ (the average aspect angle for 1980 and 1981) and used with the 1986 lightcurve in the snapshot image. For this reconstruction the rms lightcurve error converged to 0.0141. Figure 3c shows the residual between the 1986 and 1981 lightcurves and the reconstructed object lightcurves. Figure 3d uses the 1980 lightcurve alone with the 1986 lightcurve, with a rms lightcurve error that converged to 0.0126.

The image in Fig. 3a shows a significant departure from other (nonspot model) published Pluto images (Young and Binzel 1993, Buie *et al.* 1992), namely, our image does not show a bright and extended southern polar cap. The image in Fig. 3b is generally the same (subjectively) in most respects to that in Fig. 3a, but the sub-Charon hemisphere agrees better with that of Young and Binzel (1993). In particular, the bright region "B" in Young and Binzel (1993, Fig. 8) that exists in the Buie *et al.* (1992) map is present in this map. The central brightening in both Buie *et al.* (1992) and Young and Binzel (1993) can also be accommodated by the north polar region in this map. In contrast to Burwitz *et al.* (1991), who find a dark northern cap, our snapshot maps show a brighter northern region because the mean 1986 lightcurve level is slightly brighter than the mean 1981 lightcurve level, i.e., indicating that a bright and northerly feature is coming into view. The lack of a large bright southern polar cap in these maps is most probably due to the very small change in aspect angle from 1981 to 1986 which has the effect of inhibiting even large axially symmetric features from being recognized. Noise in the measurements as well as "competition" with changes near the northern pole conspire to further mask the presence of the bright southern region—which we believe is well determined to exist on the basis of past work, and in particular on the mutual event data.

Pluto lightcurves have been measured with a 2.7-m telescope (Binzel and Mulholland 1984) and the 1986 lightcurve (Buie and Tholen 1989) was acquired with the University of Hawaii 2.24-m telescope; the latter appears to be the best filled-in rotational phase lightcurve. The lightcurves in the 1980s were sufficiently close to each other in aspect, enabling Burwitz *et al.* (1991) to merge lightcurves spanning 1982–1990 for their 1D deconvolution image; they assumed a 90° aspect and showed only longitudinal variations. (Their tabulated rotational lightcurves have yet to be published, one of which was acquired in 1988 with a 2.2-m telescope.) It is interesting to note that from the mutual event lightcurves Burwitz *et al.* (1991) obtained a dark northern polar cap in contradistinction to the other published models. They also advance the view that the secular changes in Pluto's brightness, as discussed by Stern *et al.* (1988), may explain these differences.

Young and Binzel (1993) map the sub-Charon hemisphere of Pluto utilizing only mutual event data, whereas Buie *et al.* (1992) utilize both mutual event data and rotational lightcurves to map the entire surfaces of both Pluto and Charon. In the Buie *et al.* (1992) study, which accomplished the inversions with a maximum entropy technique (Skilling and Bryan 1984), there are obvious artifacts in the image and apparent feature correlation between the sub-Charon hemisphere of Pluto and the sub-Pluto hemisphere of Charon. The sub-Charon hemisphere of Pluto appears to be the "negative," or complement, of the sub-Pluto hemisphere of Charon. It is difficult to believe that such features can be real; Buie *et al.* (1993) may wish to consider performing inversions assuming a uniform Charon (until good independent Charon lightcurve measurements are available, though these data will be restricted in aspect angle coverage). Consequently, caution must be exercised concerning the detailed interpretation of the maximum entropy reconstructed surface map beyond hemispheric global variations such as a brighter southern polar region. Buie *et al.* (1992) state that the sub-Charon hemisphere of Pluto is well constrained by the mutual event data but that the anti-Charon hemisphere is poorly constrained. We argue below that this should not be the case in a unified mathematical treatment that coalesces mutual event and rotational lightcurves together in a formalism with a common object vector $\mathbf{o}$; there are constraints imposed by both the mutual event and rotational lightcurves on the anti-Charon hemisphere of Pluto. Further, highly artificial multiple-spot model simulations as used by Buie *et al.* (1992) to estimate surface map resolution have particular attributes that do not lend well as a diagnostic test of reconstruction sensitivity to the inversion of noisy data. This is discussed below.

Images from the 1970s and 1980s Lightcurves

Images were generated using the 1975, 1981, and 1986 lightcurves. Figure 4 (top) shows the spherical surface map and (bottom) the Mercator projection map. Combining the 1980 and 1981 lightcurves together yields a map that is almost identical to this map. Extensive southern

and northern polar caps appear along with albedo variations elsewhere on the planet. The diagonal structures seen in Fig. 4, exhibiting a bilateral reflection symmetry, are artifacts arising from the poor rotational phase sampling of the 1975 lightcurve. The southern polar cap arises because the mean brightness level of the 1975 lightcurve is greater than both of the 1980s lightcurves, but insufficient to drive the entire southern hemisphere into a large and uniform sea of high albedo. The sub-Charon hemisphere at 1/4 rotational phase (top, right) in Fig. 4 has a southern polar region more in concert with the Buie *et al.* (1992) and Young and Binzel (1993) images though there are disparities in the central regions of this hemisphere.

Images from the 1954–1986 Lightcurves

Next we utilize the lightcurves measured in 1954, 1964, 1980, and 1986 and the image is shown in Fig. 5a. The rms lightcurve error for this map using $\lambda = 0.0005$ is $\varepsilon = 0.0600$; with $\lambda = 0.0$ this reduces to $\varepsilon = 0.0470$. The latter value is smaller because without any smoothing the inversion fits the gross noise features in the lightcurves (particularly for 1954); however, the reconstruction of Fig. 5a remains essentially the same though the transition from light to dark regions is more more abrupt, i.e., the edges are sharper. As predicted in Section V the inversions that make use of earlier and later epoch lightcurves will (a) endeavor to squash the lightcurve variations into a tight equatorial band, (b) produce a very extensive and bright southern polar cap, (c) also generate an extensive and bright northern polar cap, and (d) cannot fit the lightcurves to being even remotely close to the noise level in the data. This last part explains why the lightcurve variations are caused by a narrow latitudinal equatorial band and exhibit very high contrast. To get the needed amplitude variations the albedo in the equatorial belt is close to zero and presented as a longitudinally stretched out "*V*" and "Λ" artifact structure. It is highly unlikely that the map in Fig. 5a depicts the true surface albedo map of Pluto; rather, it demonstrates what MLI yields when inconsistent data is furnished. Further quantitative evidence is shown by examining the residuals in Fig. 5b. The 1954 residuals are significantly above the zero mean level that would indicate that the fit was within the noise in the data. Note further that the mean 1986 residual is positive while the 1981 residual is negative. In other words, the reconstructed object cannot reconcile the brightening of Pluto prior to 1981 with the brightening that occurred after 1981.

To support this observation we generated four additional reconstructions and examined their rms lightcurve errors. The first used only 1954 and 1964; this map supported our qualitative inferences of the previous section whereby a very bright southern polar region appeared with a corrugated dark band generally above the equator. Then we generated a reconstruction using the 1954, 1964, and 1975 lightcurves, followed by 1954, 1964, 1975 and the combined 1980 and 1981 lightcurves, followed by a reconstruction using all these plus the 1986 lightcurve. After 10,000 iterations the rms lightcurve errors are 0.0237 for 1954 and 1964; 0.0475 for 1954, 1964, and 1975; 0.0488 for 1954, 1964, 1975, and the merged 1980 and 1981 lightcurve; to 0.0760 for 1954, 1964, 1975, the merged 1980 and 1981 lightcurve, and 1986. The rms lightcurve error increases as lightcurves that span a greater interval between 1954 and 1986 are used. The four reconstructions are shown in Fig. 5c. The 1954 and 1964 combination can be reasonably fitted though the reconstruction cannot in-

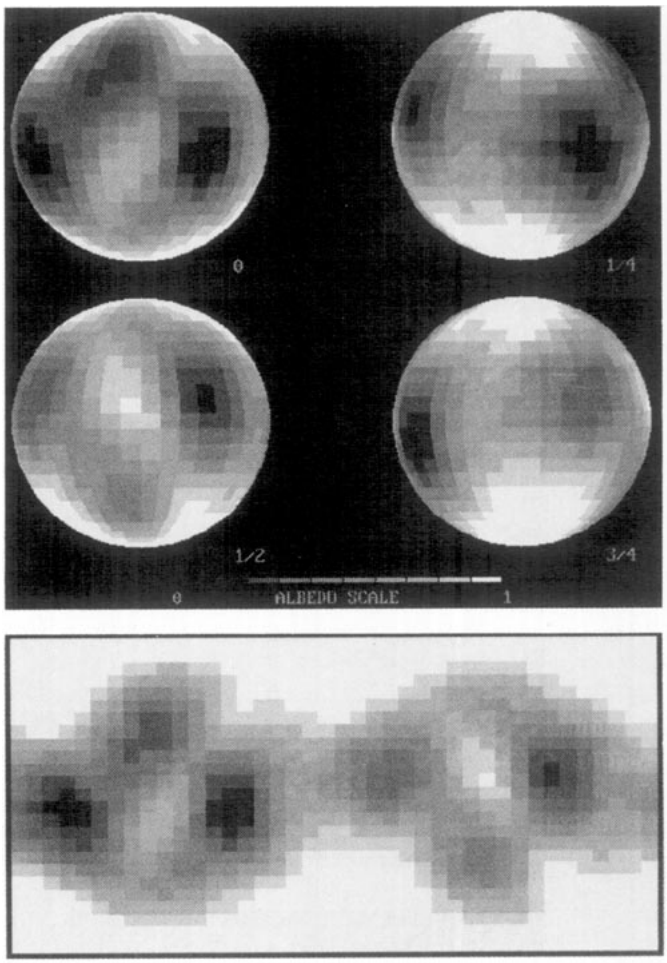

FIG. 4. (Top) Spherical map using the 1975, 1981, and 1986 lightcurves. Bright northern and southern polar regions appear because both the 1986 and 1975 lightcurves have a mean brightness greater than then 1981 lightcurve. (Bottom) Mercator map representation.

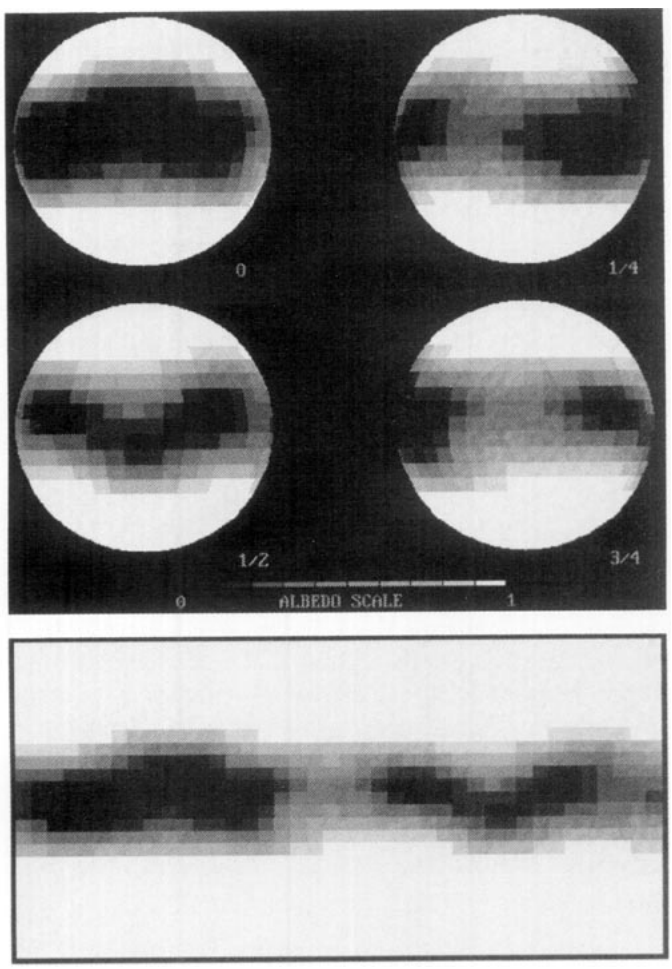

FIG. 5a. (Top) Spherical map using the 1954, 1964, 1981, and 1986 lightcurves. (Bottom) Mercator map representation.

troduce enough contrast to fit these two lightcurves to within the noise level in the data. When the lightcurves later than 1964 were incorporated a brighter northern polar region developed (which is fully out of view for the top map). When all five lightcurves are used the rms lightcurve error is the greatest because each lightcurve, as well as the mean brightness level, cannot be fit well. This is the quantitative basis for our conclusion that Pluto's surface albedo distribution has evolved over the 1954 to 1986 time frame.

There may always be questions about the state of Pluto's surface prior to the mutual event season given the quality and paucity of the data. Future questions can be answered only with the acquisition of consistent high-quality data sets closely space in time and with good rotational coverage. Were such data available from past measurements it may have been possible to create a series of snapshots showing the change in Pluto from a bright, frost-covered ball (1954–1964), through the gradual exposure of the dark layers (1972–1975), to the images shown here (1980–1986) of a relatively dark object with isolated remnants of frost.

OBJECT ERROR AND EIGENIMAGES

Terminology and Approach

We have done numerical experiments to develop an estimate, qualitatively, of the error in our reconstructed Pluto images. We outline the procedure here, for completeness sake, and then offer an opinion of the inherent risks in doing this with an unknown object utilizing MLI or any other inversion method. Although there is no technique known to the authors to estimate the true rms object error of the images shown in Figs. 3–5, without an actual resolved image of the planet, we have observed that the rms lightcurve error for a variety of simulated objects appears to be consistently and approximately log-linearly correlated with the rms object error as a function of iteration value. As the number of iterations increases the logarithms of both the rms object error and the rms lightcurve error diminish in a more-or-less linear manner.

Define the *rms object error*, to be the rms error over all surface elements between an object and its reconstruction. The *rms lightcurve error* is defined as the rms error between all points in the lightcurves associated with the

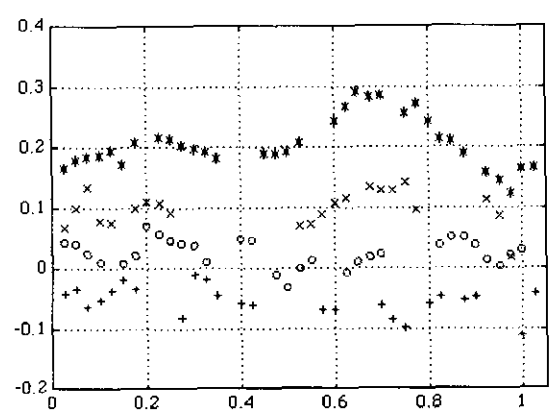

FIG. 5b. Residuals between the lightcurve fit obtained by using MLI and the four lightcurve data sets that were used in the reconstruction. Here * is the residual for the 1954 lightcurve, x the residual for the 1981 lightcurve, + the residual for the 1981 lightcurve, and o the residual for the 1986 lightcurve. The 1954 residuals are the largest ([0, π] normalized disk-integrated flux units) with a mean level far above zero; this indicates that the MLI fit could not approach the noise level in the data. Note further that the mean 1981 residual is negative while the mean 1986 residual is positive. This arises because the reconstruction could not accommodate the brightening that Pluto exhibited since 1981.

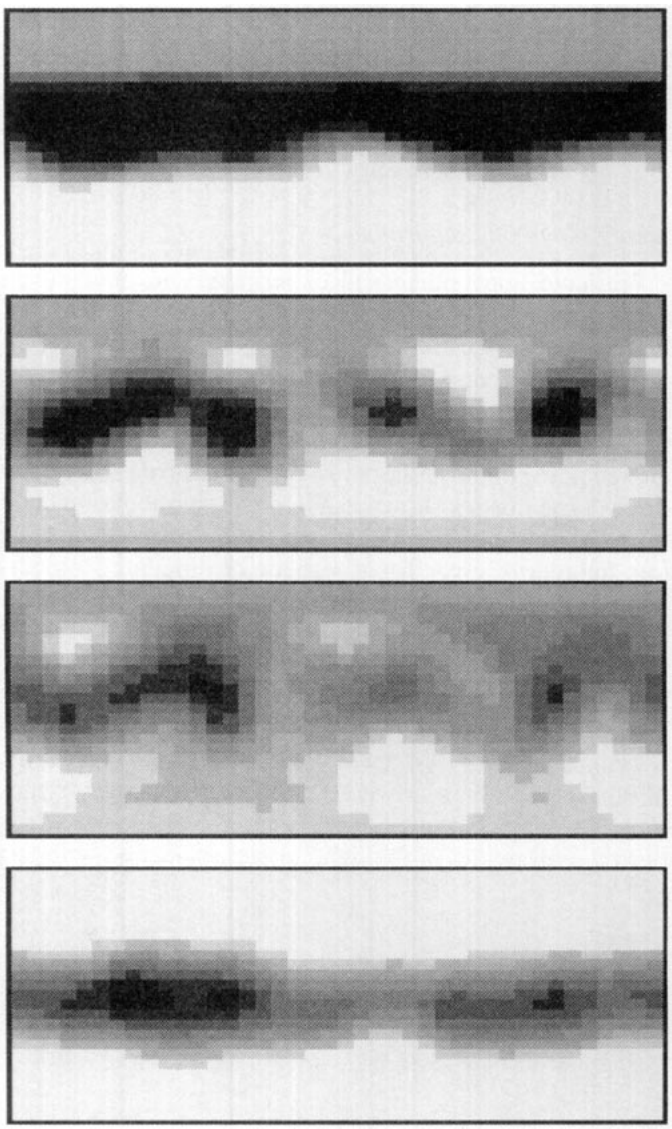

FIG. 5c. Mercator maps for 1954 and 1964 (top), 1954, 1964, and 1975 (second from top), 1954, 1964, 1975, and 1980 merged with 1981 (third from top), and 1954, 1964, 1975, 1980 merged with 1981 and 1986 (bottom). For the top map all latitudes above 36° north remain at the initial albedo value of 0.6 because they are out of view during the 1954 and 1964 epochs. A smaller polar region similarly exists in the other maps. Reconstructions that use the 1954 lightcurve all demonstrate a very large and bright southern polar region.

original object and the reconstructed lightcurves derived from the reconstructed object. In the case of a simulated object all of these quantities are *a priori* known; this is not the case for a real object such as Pluto.

The technique for Pluto proceeds as follows. First create an object, which may be a variant of the reconstructed image of Pluto, using the same M and N. Then synthesize two lightcurves from this model at the equivalent J lightcurve aspect angles. Next, invert these J lightcurves using the MLI process, using the same acceleration and smoothing constants that are used in the generation of the reconstructed image until the rms lightcurve error reaches convergence or some final cutoff value. The rms object error (between the reconstructed image and the model object) can be plotted against the rms lightcurve error (between the reconstructed lightcurves and model lightcurves), and is a parametric function of the iteration number. For our simulation experiment the resulting curve monotonically increased with the logarithm of one rms error quantity plotted against the other rms error quantity, though the curve was not perfectly linear. In other words, as, for example, the rms lightcurve error diminished the corresponding rms object error also diminished. Since the model object had lightcurves that resembled those of the measured Pluto lightcurves, we may be led to conclude similarly that as the rms error between the measured Pluto lightcurves and reconstructed object lightcurves diminishes that the rms error between our Pluto reconstructed image and the true albedo surface map of Pluto also diminishes as the iterative inversion process converges. Such an approach can lead to the dangerous assessment that the inversions are yielding images that are, in some sense, correct, when in actuality they are completely wrong.

The Eigenimage

A model object that is our starting point was created from a set of lightcurves (Fig. 6, top) and then altered by slightly enlarging the northern polar region (Fig. 6, center). The starting model object was formed from an inversion that used three Pluto lightcurves, i.e., 1981, 1982, and 1986, which were rendered to be slightly inconsistent when the choice for m_o in Eq. (10) was made (they differed from each other and from our adopted choice of m_o = 14.757). Consequently, this object has lightcurves with profiles very similar to those of Pluto, though the relative mean levels are different than the actual Pluto lightcurves. Three $M = 40$ point noiseless lightcurves were generated from the object in Fig. 6 (top) with aspect angles $\alpha_1 = 80°$, $\alpha_2 = 75°$, and $\alpha_3 = 70°$, and all three were then used in the reconstruction; the aspect angles are assumed known *a priori*. The reconstructed image generated using MLI is shown in Fig. 6 (center). The iterations proceeded until the rms error between the model object lightcurve and reconstructed object lightcurve, defined by Eq. (7), reached $\varepsilon = 0.0010$.

Were the original object formed entirely from random "brushstrokes" one can be pleased at the quality of the reconstruction shown in Fig. 6 (bottom). If this image were shown as an example of the efficacy of MLI to an

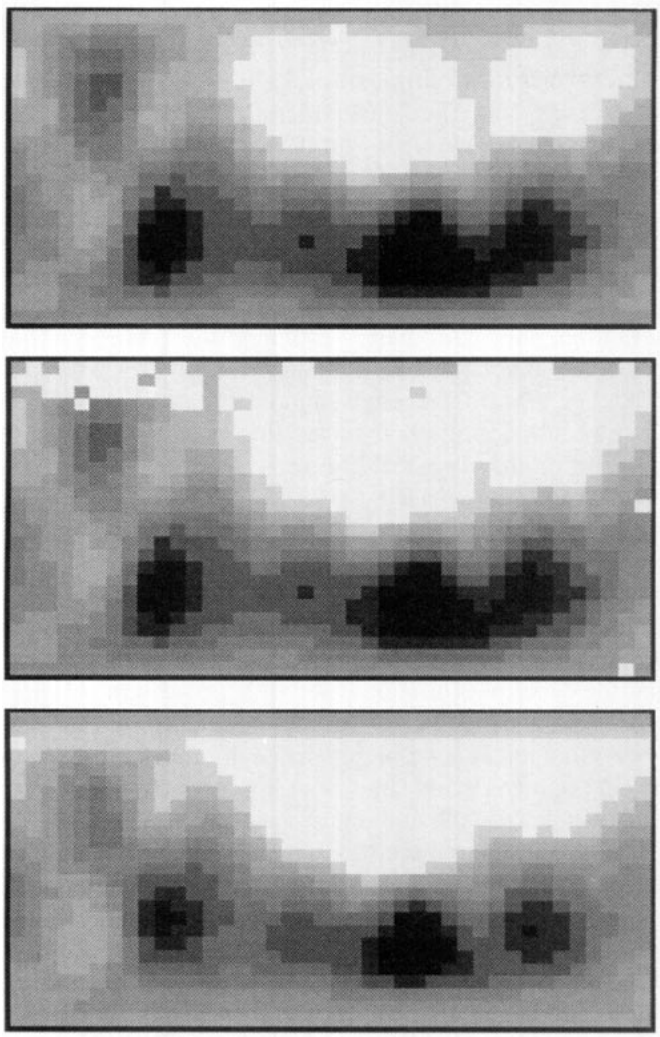

FIG. 6. (Top) The original eigenimage object, generated from inconsistent Pluto lightcurves. (Center) The slightly modified eigenimage; most changes were made in the polar region. (Bottom) The reconstructed eigenimage map using two lightcurves generated from the center map. In general this reconstruction is an excellent rendition of the original object (top or center objects).

uninformed observer, a totally incorrect conclusion as to the capability of MLI would be drawn. It is risky to conclude the MLI works spectacularly based on this, or a similarly developed, simulation. Similar statements can be made about any inversion technique. Because the model object was basically fashioned from a set of given lightcurves (with very slight changes) we have used an object that is in the neighborhood of an *eigenimage* of the system matrix **H**. In other words, any reconstructed object, regardless of the input lightcurves, is an eigenimage if the same reconstructed object lightcurves are used as the inputs to the inversion process. Since we began with a model object that was derived from our original Pluto reconstruction, to enable us to have model object lightcurves very similar in form to the actual Pluto lightcurves, it is not surprising that our simulated model object was reconstructed so well.

Another difficulty in estimating the rms error between the reconstructed object and true planet surface map is that, at least in the absence of [0,1] albedo boundedness constraints and smoothing, it can easily be shown (Harmon *et al.* 1993) that inversions exist that fit the noiseless lightcurves to arbitrarily high precision but which have a very large rms object error, particularly as we increase N and M. In the presence of albedo positivity or boundedness constraints which forces more continuous or smoother solutions to be accepted this problem is much less severe. The unconstrained iterations in Eq. (6a) will converge to the least-squares inverse solution; constrained solutions will generally converge to other, perhaps distant, regions in the solution space. There may exist other, less smooth, solutions that replicate the lightcurve data and satisfy the imposed constraints, i.e., albedo constrained within the unit interval [0,1] for our simulations. If it can be proved that such other solutions exist in some sense close to the reconstruction, i.e., within some small neighborhood of the solution point corresponding to the constrained iterative inversion, then it may be possible that the rms object error can be functionally (or monotonically) and hence quantitatively correlated as the iterative solution converges with the true rms lightcurve error.

SIMULATIONS AND INFERRING SURFACE RESOLUTION

Highly Artificial Multiple Spot Model

Figure 7a is a Mercator projection map of a simulated object with a background albedo of 1.0 that has four spots

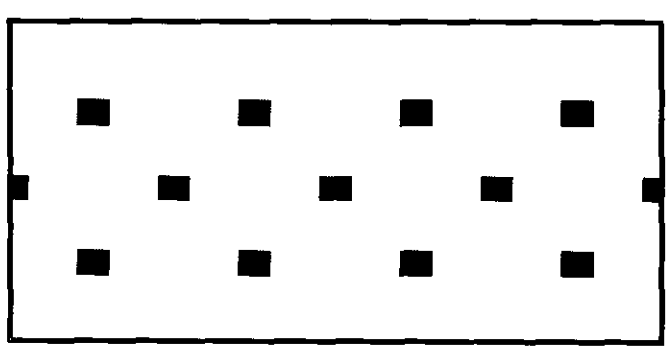

FIG. 7a. The 12-spot artificial object. Each spot has unity albedo and extends over a 2 × 2 pixel region; the background albedo is set at 0.1.

comprising 2 × 2 surface pixel regions with zero albedo in each of three latitudinal bands. The central band of spots is out of phase longitudinally with the mid-latitudinal band of spots. This is a highly structured object analogous to that used by Buie *et al.* (1992) in their simulation, though we ignore generating a simultaneous surface map for Charon. This multispot model is not an eigenvector of the matrix **H**. The noiseless lightcurves are shown in Fig. 7b (top) for four aspect angles consisting of $\alpha = 93°$, $\alpha = 103°$, $\alpha = 134°$, and $\alpha = 144°$ in analogy with the 1986, 1981, 1964, and 1954 Pluto aspect angles, respectively. In 7b (center) is the equivalent set of four lightcurves degraded with modest levels of Gaussian-distributed random noise, while Fig. 7b (bottom) shows the high noise level lightcurves.

Figure 8a shows the MLI reconstructions using the noiseless lightcurves with from one to all four lightcurves used in the reconstruction. Figure 8b shows the reconstructions for the moderately noisy lightcurves, while Figure 8c presents the reconstructions using the high noise level lightcurves. The single lightcurve reconstructions (bottom image) use the $\alpha = 134°$ lightcurve, the two-lightcurve reconstructions use the $\alpha = 93°$ and $\alpha = 134°$ lightcurves, and the fourth reconstruction (top image) uses all four lightcurves. For all the noisy lightcurves we used a smoothing parameter of $\lambda = 0.00025$ and for all cases we performed 125,000 iterations. Such a large number of iterations was needed most for the four-lightcurve case, but also was required because of the sinusoidal nature of the lightcurves (evident in Fig. 7) caused by the azimuthal spot periodicity. Although the rms lightcurve error for the noiseless lightcurves asymptotically approaches zero in the limit of infinite iterations, for our chosen cutoff the rms error for the four lightcurve case was approximately 0.13% and approximately 0.02% when one lightcurve was used.

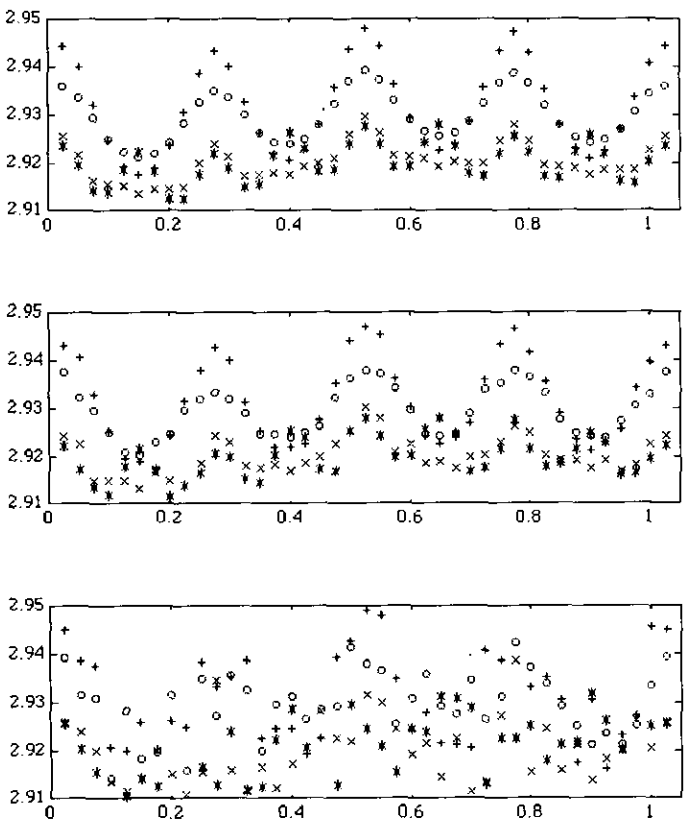

FIG. 7b. (Top) The four noiseless lightcurves generated from the 12-spot object. Here * has the same aspect as 1954, x as 1964, + as 1981, and o as 1986. (Center) The same four lightcurves with moderate Gaussian noise added to each lightcurve. (Bottom) The same four lightcurves with substantially more Gaussian noise added to each lightcurve. The vertical scale is in disk-integrated flux units normalized to the interval $[0, \pi]$.

Consider the results in Fig. 8a, and in particular the case where only two lightcurves consisting of 80 data points are used to reconstruct 1000 surface elements. This does a very reasonable job of specifying where all the spots are localized, though they are slightly blurred out and the dark spots are not at zero albedo as in the original object. Part of the reason for this, perhaps surprising, feat is that the object is so highly artificial, and the multispot object produces many sinusoidal ripples in the lightcurves as the spots move in and out of view. Using three or four lightcurves rendered reconstructions that appear to differ little from when two lightcurves were used. Because we cut off the iteration process at 125,000, the four-lightcurve reconstruction demonstrates slightly poorer quality than the two- or three-lightcurve case because of its slower rate of convergence; the speed of convergence diminishes with increasing numbers of lightcurves. Also, the use of a single lightcurve partially recovers the equatorial spots and southern latitude spots and shows an indication of the mid-latitudinal northern spots, which are almost out of view for the chosen aspect angle. The four-lightcurve case took about 1 day of processing time on a 486 33-Mhz PC system.

Figure 8b shows the corresponding four reconstructions for the moderately noised lightcurves. These reconstructions localize the spot positions well though the spots themselves are of slightly less contrast and a little more blurred out. The reason for the good localization lies in the use of a multispot object itself which give rise to high-frequency sine-wave type lightcurves. Because the noise is of higher frequency but lower amplitude and superimposed on the low-frequency high-amplitude spot-induced signal, it will have little effect on the reconstruction until the primary signal is fitted. The sinusoidal structure alone reveals the presence of localized spots on the surface; the model is so highly artificial, in fact, that drawing conclusions about general performance characteristics (such as surface resolution) cannot be realized.

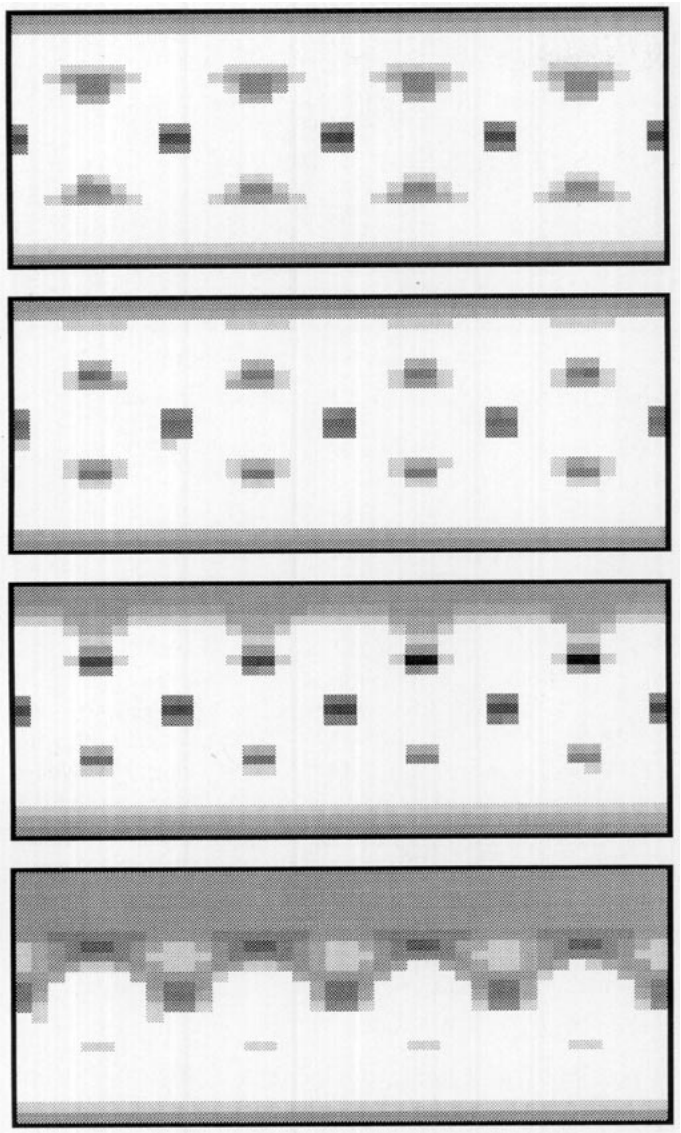

FIG. 8a. Reconstructions of the 12-spot object using the noiseless lightcurves. The top map used all four lightcurves; the second map used three lightcurves with aspects angles of 93°, 103°, and 134°; the third map uses two lightcurves with aspect angles of 93° and 134°; the bottom map uses a single lightcurve with aspect angle of 134°.

For the high-noise lightcurves shown in Fig. 7d, the reconstructions in Fig. 8c continue to localize the spot features, though the spot shapes have diminished in quality from the moderate noise case. The noise amplitude is now comparable to the spot signal amplitude in the lightcurves. Clearly, the very artificial nature of this simulation can lead to a highly misleading estimate of the resolution of an inversion technique because a similar noise level in the lightcurves of a more realistic object model will lead to reconstructions bearing no similarity at all to the original object.

A multispot model was utilized by Buie *et al.* (1992) where they inferred the surface resolution attainable over part of the mapped surface for the maximum entropy method. From the present investigations it appears that any conclusion drawn about reconstructed surface resolutions from multispot models must be reexamined. The attainable surface resolution that can be obtained with inversion techniques such as MLI will be object as well as data dependent. The former case arises because many different surface configurations will fit a given lightcurve. When more than one lightcurve is used at different aspects, solar phase angles, or color-dependent limb darkening effects, the ill-posedness diminishes and the resolution attainable becomes more data dependent (Harmon 1995). The use of positivity and smoothing narrows the accept-

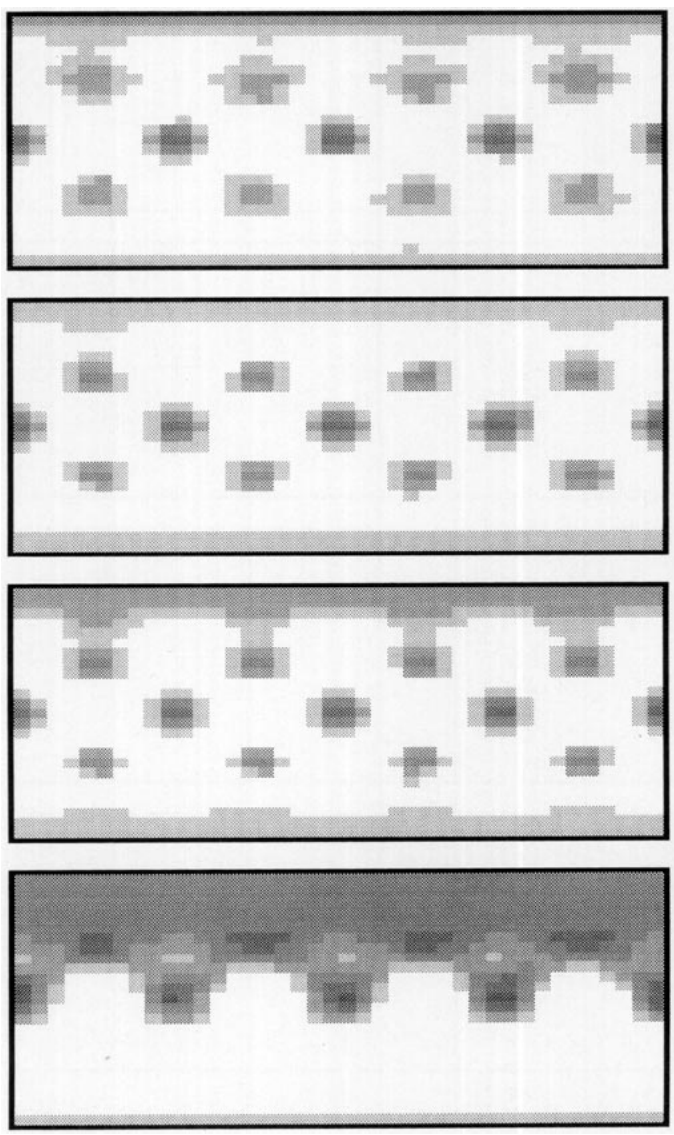

FIG. 8b. Reconstructions using the moderately noisy lightcurves. The maps are oriented identically to those in Fig. 8a. All 12 spots are recovered in this map.

able set of solutions to uniqueness so that resolution may be definable in terms of the "modes" that can be reconstructed; these can be spherical harmonics. This is a vital topic for future research because to reach a given surface resolution imposes conditions on the quality and quantity of the measured data that must be met (Harmon 1994).

Plausibly Realistic Object

Figure 9a shows a more continuous simulated object that is plausibly realistic. It was fabricated using random "brushstrokes" and subsequent smoothing to fully avoid the possibility of it being an eigenimage. Figure 9b (top) shows the four noiseless lightcurves for this object; they correspond to the four Pluto aspect angles used in the previous multispot simulation. Figure 9b (bottom) shows these lightcurves degraded with different levels of noise.

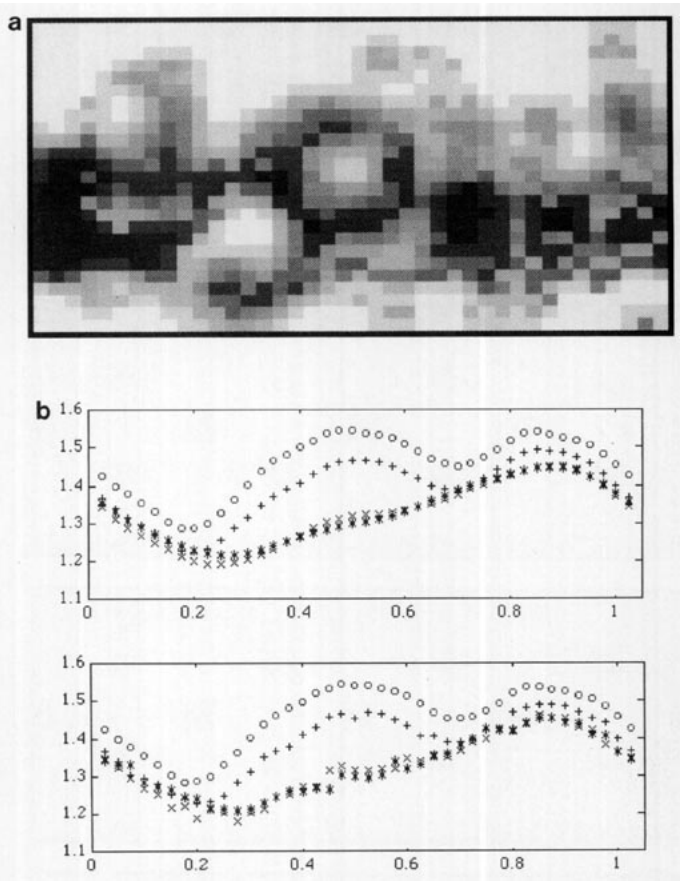

FIG. 9. (a) Plausibly realistic simulated object. (b) (Top) The noiseless lightcurves with aspect angles corresponding to Pluto for 1954 (8), 1964 (x), 1981 (+), and 1986 (o). (Bottom) The lightcurves with varying degress of Gaussian random noise added.

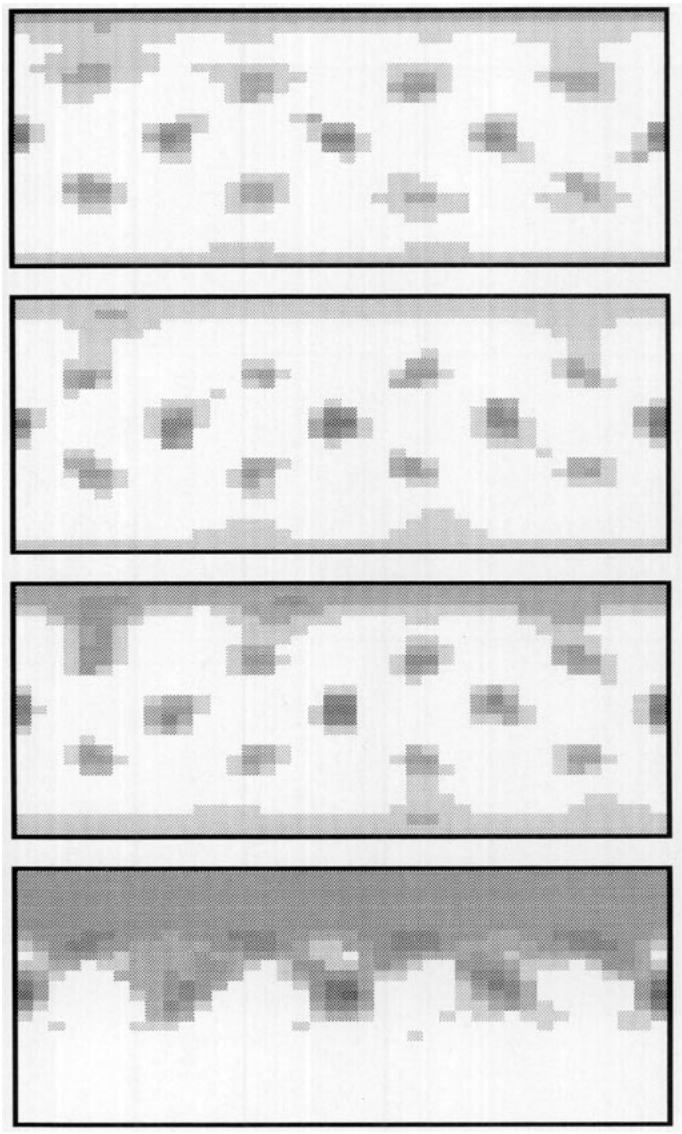

FIG. 8c. Reconstructions using the high-noise lightcurves. The maps are oriented identically to those in Fig. 8a. Note that the 12 spots, though slightly blurred out, are still evident. This indicates that the highly artificial multispot simulations are a misleading indicator of spatial surface resolution for lightcurve inversion procedures.

Figure 10a shows the ensemble of reconstructions using from one to all four noise-free lightcurves simultaneously; the images are shown analogously to the above multispot simulations. Figure 10b show the reconstructions for the noisy lightcurves. The subjective interpretation from these results is that in the noiseless case the three- and the four-lightcurve reconstructions do a remarkably good job at recovering the major prominent features. The two large crater-type regions are recovered as well as the locations for the boundaries of the various other features though the dark spot at rotational phase 0.8 has not been recovered. When noise is added the finer features are lost, though there remain similarities to the original object.

The set of aspect angles used in these simulations are chosen to reflect those of Pluto. Simulated objects—and presumably real objects too—will be better reconstructed

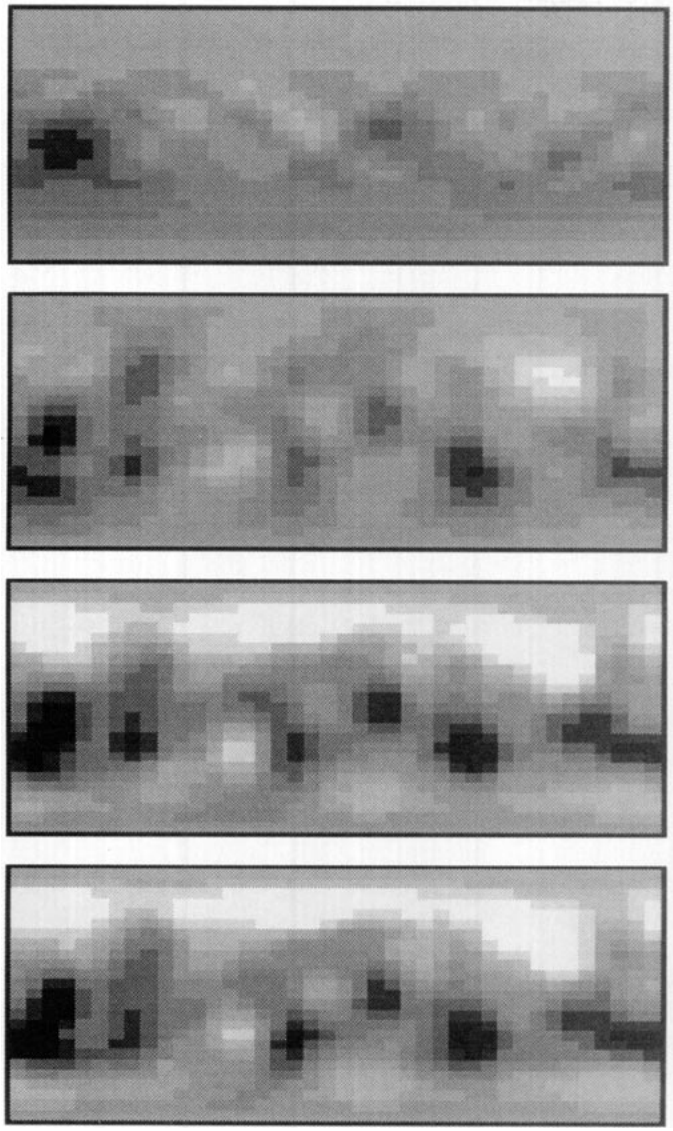

FIG. 10a. Series of four reconstructions of the object in Fig. 9a using between one and four noiseless lightcurves. The top reconstruction uses one lightcurve with $\alpha = 134°$; the second reconstruction uses two lightcurves with $\alpha = 93°$ and $\alpha = 134°$; the third reconstruction uses three lightcurves with $\alpha = 93°$, $\alpha = 134°$, and $\alpha = 103°$; the bottom reconstruction uses all four lightcurves.

were the lightcurves measured over a greater range of aspect angles and perhaps if more lightcurves were available. Though our inferences from simulations indicates that little advantage is gained as the number of lightcurves is simply increased beyond a few. That is, the quality of the reconstructions appears to be a stronger function of the sampling and spacing over the range in aspect angle than of number of lightcurves, J, over a given range of aspect angles. Also, as the number of lightcurves J increases the convergence rate dramatically slows down and more computer time is needed to get images with an identical rms lightcurve error to a reconstruction with fewer lightcurves. This is a drawback of the simple Jacobi method that can be overcome using more sophisticated iterative techniques such as conjugate gradient descent.

Image Quality

It is important to distinguish between making qualitative or subjective versus quantitative judgments of image quality based on a handful of simulations. The "standard" scenario consists of showing results utilizing enhancements, reconstructions or inversions, deconvolutions, etc., of the image and offers the audience a subjective assessment of the performance of the technique. Such qualitative characterizations are necessarily biased be-

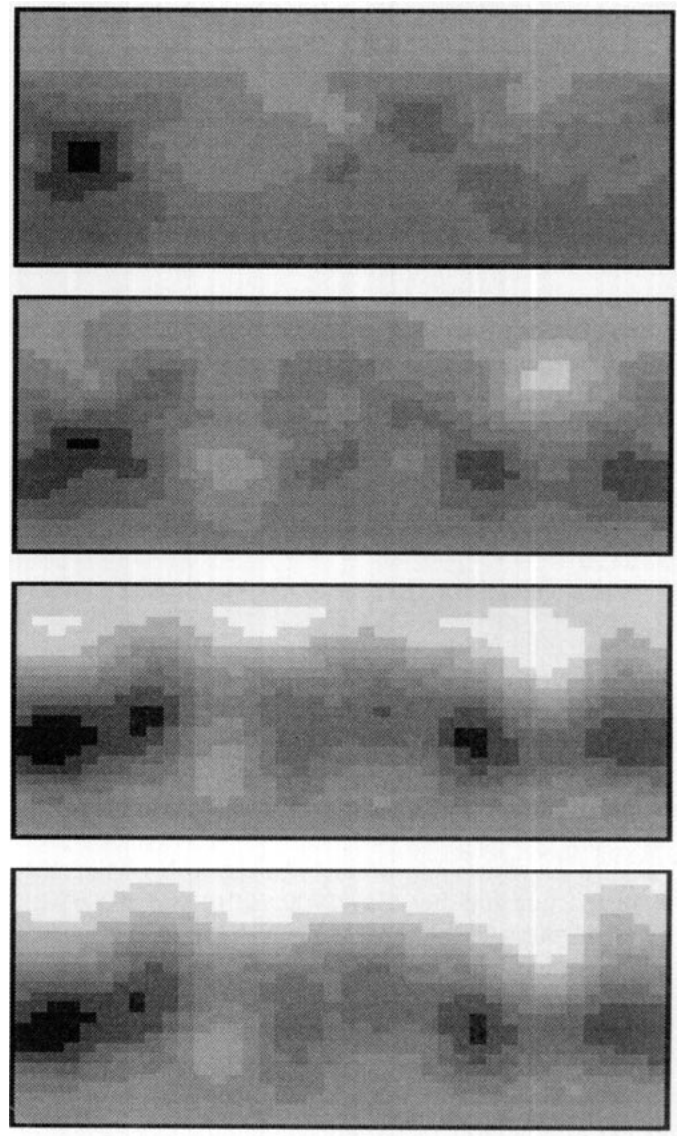

FIG. 10b. Reconstructions using the noisy lightcurves, with aspect angles and number of lightcurves as indicated in Fig. 10a.

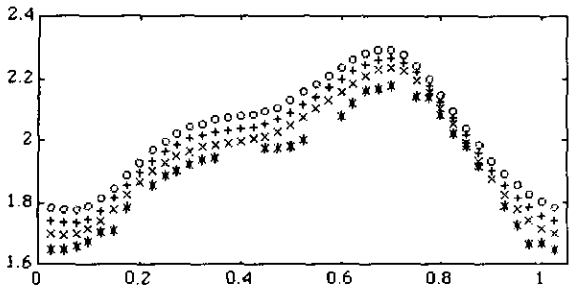

FIG. 11. Predicted Pluto lightcurves for 2000 (x, $\alpha = 84°$), 2010 (+, $\alpha = 78°$), and 2020 (o, $\alpha = 72°$) generated using the reconstructed surface map in Fig. 3b. The 1986 (*, $\alpha = 93°$) lightcurve from this reconstruction is shown for comparison.

cause of the nature of the human observer. Barrett (1990) offers a quantitative treatment concerning the objective assessment of image quality, though it appears to be a difficult process. We are perhaps also guilty of pursuing the purely subjective approach, though part of our effort has been to verify inconsistencies in the data and thus furnish evidence of a nonstatic surface. The motivation behind the recognition of the importance of eigenimages was based on numerical experiments to quantitatively estimate rms object error through a correlation with rms lightcurve errors; this turned out to be an incorrect approach. Error propagator maps can easily be misunderstood because they indicate only where the data are weak (or excessively noisy) and the degree of mathematical constraint in reconstructing pixels over the planet's surface. These error maps say little, if anything, in regard to how close the reconstructed maps agree with the actual surface of Pluto.

PREDICTED LIGHTCURVES AND SURFACE EVOLUTION

We can offer predictions of how Pluto's lightcurves will evolve under the static surface assumption. We choose the snapshot reconstruction in Fig. 3b for our predictions because of the quality of the data used and our assessment of the reconstruction being reasonably consistent with the sub-Charon maps shown in Young and Binzel (1993, Fig. 8).

Figure 11 shows the predicted lightcurves using this reconstruction for the years 2000, 2010, and 2020, with the 1986 lightcurve (as generated from the reconstruction) as a reference. These choices assumed a linear change in aspect angle of $\Delta\alpha = 0.627°$/year. The vertical scale is disk-integrated surface brightness normalized to π. Note that the lightcurves increase in brightness with little change in the overall structure. The peak position shifts slightly in rotational phase and a minimum develops near zero rotational phase. The "shelf" structure remains more-or-less intact, though perhaps is slightly more pronounced. When we did a similar analysis using the object in Figs. 4a and 4b—the map using 1975, 1981, and 1986—the "shelf" feature slowly blended away with time.

Pluto is presently moving away from the Sun after having passed perihelion in 1989 so the solar insolation is diminishing with, presumably, a resultant cooling of the atmosphere and as Stern *et al.* (1988) suggests the methane will begin to precipitate out of the atmosphere and cover Pluto's surface in some uneven pattern and therefore convert Pluto into a bright snowball again. The brightening in our predicted lightcurves is caused by the northern polar region moving further into view. One might suspect that methane frosts will even further enhance the surface albedo of Pluto's surface in excess of that predicted in Fig. 11. As the methane frost covering proceeds, the amplitude variation will probably diminish for two reasons: (1) the aspect angle diminishes so that the northern polar region persists in view over all rotational phases analogous to the 1954 situation when the southern polar region was persistently in view and (2) the frost formation will brighten up those areas that are dark and hence diminish their contribution to the lightcurve amplitude variations. In Young and Binzel (1993) and Binzel (1992) a physical explanation of the bright southern polar region is put forward based on the requirement to maintain a constant global temperature through the release of energy via the latent heat of condensation while the southern polar area receives no solar insolation. Consequently, the northern polar region may either remain static, or may actually diminish in size though Pluto is receding from the Sun. In the former case this may be attributable to the frost formation occurring primarily in the southern regions that are getting no solar insolation. Pluto is still close to perihelion for the next ~20–30 years, so the reduction in solar insolation may be such that what frosts form or snow-like precipitation from the atmosphere occurs (atmospheric freezeout) will take place near the south pole. In this case our lightcurve predictions may be reliable as the static surface assumption is more-or-less valid over most of the surface in view. In the latter case the north polar region may diminish in extent precisely because Pluto is still in the vicinity of perihelion and given the approximately one decade thermal lag time the northern frosts will sublimate perhaps at the same time that the southern polar region receives its frost covering. In other words, Pluto's atmosphere may be undergoing some rather complex dynamics in those epochs before and after its passage through perihelion. The ability to obtain and properly interpret, i.e., invert, the various multicolor lightcurves is therefore of extreme importance and significance for correctly ironing out the details of the dynamic global properties of atmospheric transport on Pluto.

We have adopted the view of Stern *et al.* (1988) that the reason for a dynamically changing surface is due to

the sublimation, mobility, and freezeout of atmospheric methane. However, recent observations of Owen *et al.* (1993) indicate that the primary surface ice and atmospheric constituent on Pluto is N_2 and is approximately 50 times more abundant than CH_4 and CO. Owen *et al.* (1993) also point out that the surface pressure and temperature of Pluto may be near the triple point of N_2, which implies that there may be some very complex surface dynamics in regard to the mixing and distribution of these volatile ices as Pluto passes through its perihelion passage when solar insolation is the greatest and present over the entire disk of the planet.

INCORPORATING MUTUAL EVENTS INTO THE FORMALISM

Since Eq. (3) is linear it can be used in tandem with other linear estimation procedures, such as the inversion of mutual event lightcurves (Brinkmann 1976), if the same polyhedral surface discretization and physical basis is used for the object vector **o**. The unified rotational and mutual event lightcurve formulation (Wild 1993, unpublished notes) is summarized here as we feel it important to let others be aware of this approach. The mutual event data is concatenated to the column data vector **d**, to get the augmented vector **d***,

$$\mathbf{d}^* = \begin{bmatrix} \mathbf{d}_{RL} \\ \mathbf{d}_{ME} \end{bmatrix}, \tag{12a}$$

where the subscript "RL" refers to rotational lightcurves and "ME" to mutual event lightcurves. The mutual event lightcurve data is sampled with an incremental motion of Charon (and its shadow) of one sub-Earth longitudinal pixel, similar to that used in MLI, (the usage of "sub-Earth" indicates a pixel size corresponding to the largest projected longitudinal extent), and as finely and irregularly as is desired recognizing below that elements in the transfer matrix **H** may be fractional facet areas. An adequately fine surface discretization can be used to offset undesired partial pixel obscuration effects around the limb of Charon and its shadow projected upon Pluto. The augmented matrix, designated as **H***, consists of the rotational version as given by Eq. (4c), followed by rows that have entries that are zero for all surface patches on the anti-Charon hemisphere of Pluto, zero for those patches obscured by Charon and its shadow, and the same ξ_{ij} for those patches in full view, and some fraction of this projected area for pixels that are only partially obscured for well sampled data in the mutual event phase domain. The matrix **H*** has the form

$$\mathbf{H}^* = \begin{bmatrix} \mathbf{H}_{RL} \\ \mathbf{H}_{ME} \end{bmatrix}. \tag{12b}$$

Each additional row of **H** corresponds to a specific position of Charon relative to Pluto. The uniform illumination contribution from Charon itself is included via the mean Pluto magnitude preceding and following the mutual event lightcurve diminution, i.e., the 0.167 (or other adopted value, depending on the color index) magnitude factor that we subtracted out for our analysis is automatically included in the mutual event data.

The structure of **H*** with **d*** furnish constraints upon **o**, i.e., the nullity of **H*** is smaller than the nullity of **H**. The rotational lightcurves can be characterized as the output of an integrating filter (see Eq. (11)), whereas the mutual event lightcurves are the output of a differentiation filter. For instance, as Young and Binzel (1993) noted, albedo variations present on Charon will have little effect on the mutual event lightcurve because it is a constant background during the interval of the eclipses. That is, from one measurement to the next small portions of Pluto's surface are covered and then uncovered, while most of the surface is a constant background source. For the rotational lightcurves the entire surface is modulated with respect to the template sphere; this is not the case with the mutual events. There are fundamental differences between how rotational and mutual event lightcurves are formed, so the simultaneous inversion of these two data sets will furnish the best possible snapshot images for Pluto in the 1980s. Interestingly, the mutual event lightcurves will also constrain the anti-Charon hemisphere of Pluto because the rotational lightcurves integrate over projected disks for those rotational phases that show only portions of the sub-Charon hemisphere. This constraint carries over to the anti-Charon hemisphere of Pluto. Consequently, the "reality" of the entire surface map should improve for a snapshot image that incorporates mutual events as well as rotational lightcurves acquired during the 1980s.

CONCLUSIONS

Pluto represents an almost ideal application of matrix lightcurve inversion. This is because it is a spherical body with a known pole orientation, inferred from the orbit of Charon, so the aspect angle is well established throughout its orbit. Additionally, it has a large obliquity and its solar phase angle is negligible ($\leq 1.9°$) whereby the lightcurves can be reduced to a common viewing geometry with Pluto always at opposition so that the geometric scattering assumption may be valid. Also, of course, Pluto demonstrates intriguing lightcurve variations, which have changed substantially since they were first measured in 1954. Few of these characteristics hold true for most asteroids or satellites in the Solar System.

We assumed that Charon is featureless and is therefore a removable background for all lightcurves. Recent work

by Olkin *et al.* (1993) and Buie and Shriver (1994) support this assertion, though small albedo variations on Charon will not affect our conclusion that Pluto's surface has undergone evolutionary changes from 1954 to 1986. Color-dependent photometry, adaptive-optics-compensated imagery, and HST observations will enable the individual Pluto–Charon lightcurves to be decoupled and will instigate a new hierarchy of reconstructions. Continuing observations will be invaluable for monitoring active volatile transport over the surface through and beyond Pluto's perihelion passage.

Snapshot images of Pluto can be attained utilizing lightcurves acquired several years apart, corresponding to small changes (~10°) in the aspect angle, though reliable reconstructions require the highest possible data quality. Otherwise there is a risk of losing axially symmetric features because of noise masking the small changes in the orbital lightcurve. However, it is partically impossible to acquire densely sampled lightcurves over the full rotational phase during any single observing session at a large-aperture telescope to attain the needed precision for snapshot images using lightcurves taken just years apart. The motivation leading to snapshot reconstructions originated because of the inconsistency between lightcurves over 1954 to 1986, and because the lightcurves from the 1980s were deemed of satisfactory quality for demonstrating the principle. Inversions that combine the 1980s data with data from the 1970s leads to unreal-appearing maps probably induced by the high noise level and large gaps in the 1970s rotational phase coverage.

The matrix formalism for lightcurve inversion enables use of the many tools of ill-posed estimation theory for performing the inversions; we choose to use a simple constrained iterative technique. This is a vast body of literature on regularization theory applied to ill-posed inverse problems analogous to that treated here (see, for example, Morozov 1984, Root 1987, Tikhonov and Goncharsky 1987, Turchin *et al.* 1971, Twomey 1963, 1977). MLI is easily generalized to accommodate wavelength-dependent limb darkening effects (Harmon, unpublished communication, 1993, Wild *et al.* 1994) and more general surface scattering laws than geometric scattering.

There is a substantial body of existing Pluto and Charon lightcurve data which embodies multicolor rotational and mutual event photometry and more recently groundbased and HST-acquired separated Pluto and Charon rotational lightcurves (Binzel 1993, personal communication). The reduction and organization of these data is an ongoing task, and once this database becomes available to the greater community revised surface maps should be developed using the many techniques available. Only in this manner can increased confidence in some of the more salient features on the surface be obtained and confidently be used for surface–atmospheric interaction studies.

It is desirable to acquire high-quality lightcurves of Pluto and Charon spaced ~2–3 years apart to enable the generation of snapshot images. Dynamical variations of the planet's surface from atmospheric transport of volatiles can then be better understood; these can be consolidated with atmospheric and meteorological models, which in turn are corroborated by stellar occultation measurements. For a minuscule fraction of the cost of a space mission to Pluto, HST or large-aperture telescope time periodically dedicated to acquiring multicolor full rotational phase coverage of Pluto and Charon will be of inestimable scientific value to future researchers attempting to reconstruct Pluto's evolving surface and atmosphere. These observations will be particularly critical because Pluto's aspect angle has recently passed below the 90° point, and these data will shed light on the evolution of the postulated bright southern polar region. Furthermore, the surface maps will enable space mission planners to optimize spacecraft reconnaissance trajectories to maximize scientific return (Stern 1993). Coordinated observational programs should be seriously considered by members of the Pluto community as it will be the only way to get moderately high-resolution images for many years to come.

ACKNOWLEDGMENTS

The authors acknowledge very useful discussions with Professor Robert Rosner. W. Wild thanks Professor Edward Kibblewhite for helpful discussions and for his generous support of this project, Dr. Steve Ostro for his encouragement to continue to apply the matrix lightcurve inversion technique, and Dr. Rickey Pastor for his insightful suggestions.

REFERENCES

ANDERSSON, L. E., AND J. D. FIX 1973. Pluto: New photometry and a determination of the axis of rotation. *Icarus* **20,** 279–283.

BARRETT, H. H. 1990. Objective assessment of image quality: Effects of quantum noise and object variability. *J. Opt. Soc.* **A7,** 1266.

BINZEL, R. P. 1988. Hemispherical color differences on Pluto and Charon. *Science* **241,** 1070–1072.

BINZEL, R. P. 1992. 1991 Urey Prize lecture: Physical evolution in the solar system—present observations as a key to the past. *Icarus* **100,** 274.

BINZEL, R. P., AND J. D. MULHOLLAND 1984. Photometry of Pluto during the 1983 opposition: A new determination of the phase coefficient. *Astron. J.* **89,** 1759–1761.

BRINKMANN, R. T. 1976. On the inversion of mutual occultation light curves. *Icarus* **27,** 69–89.

BUIE, M. W., AND S. K. SHRIVER 1994. The distribution of water frost on Charon. *Icarus* **108,** 225–233.

BUIE, M. W., AND D. J. THOLEN 1989. The surface albedo distribution of Pluto. *Icarus* **79,** 23–37.

BUIE, M. W., D. J. THOLEN, AND K. HORNE 1992. Albedo maps of Pluto and Charon: Initial mutual event results. *Icarus* **97,** 211–227.

BURWITZ, V., K. REINSCH, M. W. PAKULL, AND P. BOUCHET 1991. New aspects of the binary planet Pluto–Charon. *ESO Messenger,* December, pp. 23–26.

CAMPBELL, S. L., AND C. D. MEYER 1991. *Generalized Inverses of Linear Transformations*. Dover, New York.

CHRISTY, J. W., AND R. S. HARRINGTON 1978. The satellite of Pluto. *Astron. J.* **83,** 1005–1008.

DAVIS, P. J. 1979. *Circulant Matrices*. Wiley, New York.

DRISH, W. F., R. HARMON, W. J. WILD, AND R. L. MARCIALIS 1993. Pluto images generated via matrix lightcurve inversion. *Pluto–Charon Conference Proceedings,* Flaggstaff, AZ, July 6–9, 1993, p. 22.

EATON, J. A., AND D. S. HALL 1979. Starspots as the cause of the intrinsic light variation in the *RS Canum Venaticorum* type stars. *Astrophys. J.* **227,** 907.

FRENCH, L. M., AND J. VEVERKA 1983. Limb darkening of meteorites and asteroids. *Icarus* **54,** 38–47.

GINDI, G. R., R. G. PAXMAN, AND H. H. BARRETT 1984. Reconstruction of an object from its coded image and object constraints. *Appl. Opt.* **23,** 851–856.

HARDIE, R. H. 1965. A re-examination of the light variation of Pluto. *Astron. J.* **70,** 140. [Abstract]

HARMON, R., W. WILD, R. ROSNER AND W. DRISH 1993. Starspot reconstruction via matrix lightcurve inversion. Bull. *Am. Astron. Soc.*

HARMON, R. 1995. Ph.D. dissertation, University of Chicago.

JENNINGS, A., AND J. J. MCKEOWN 1992. *Matrix Computation*. Wiley, Chicester.

KILADZE, R. I. 1967. Physical parameters of Pluto. *Sol. Sys. Res.* **1,** 173–175.

KILADZE, R. I., AND V. J. KUKHIANIDZE 1992. Two-color photometry of Pluto. *Sol. Sys. Res.* **25,** 330–332.

LACIS, A. A., AND J. D. FIX 1971. Lightcurve inversion and surface reflectivity. In *Physical Studies of Minor Planets* (T. Gehrels, Ed.), NASA SP-267, pp. 141–146.

LACIS, A. A., AND J. D. FIX 1972. An analysis of the light curve of Pluto. *Astrophys. J.* **174,** 449–452.

LANE, W. A., J. S. NEFF, AND J. D. FIX 1976. A measurement of the relative reflectance of Pluto at 0.86 microns. *Publ. Astron. Soc. Pac.* **88,** 77–79.

LUCY, L. B. 1992. Statistical limits to superresolution. *Astron. Astrophys.* **261,** 706–710.

LUENBERGER, D. G. 1969. *Optimization by Vector Space Methods*. Wiley, New York.

MAGNUSSON, P., M. A. BARUCCI, J. D. DRUMMOND, K. LUMME, S. J. OSTRO, J. SURDEJ, R. C. TAYLOR, AND V. ZAPPALA 1989. Determination of pole orientations and shapes of asteroids. In *Asteroids II* (R. P. Binzel, T. Gehrels, and M. S. Matthews, Eds.) pp. 67–97 Univ. of Arizona Press, Tucson.

MARCIALIS, R. L. 1983. *A Two-Spot Model for the Surface of Pluto*. Master's thesis, Vanderbilt University, Nashville, TN.

MARCIALIS, R. L. 1988. A two-spot albedo model for the surface of Pluto. *Astron. J.* **95,** 941–947.

MARCIALIS, R. L. 1990. Ph.D dissertation, University of Arizona.

MARCIALIS, R. L., AND L. A. LEBOFSKY 1991. CVF spectrophotometry of Pluto. *Icarus* **89,** 255–267.

MOROZOV, V. A. 1984. *Methods for Solving Incorrectly Posed Problems*. Springer-Verlag, New York.

NEFF, J. S., W. A. LANE, AND J. D. FIX 1974. An investigation of the rotational period of the planet Pluto. *Publ. Astron. Soc. Pac.* **86,** 225–230.

NULL, G. W., W. M. OWEN, AND S. P. SYNNOTT 1993. Masses and densities of Pluto and Charon. *Atron. J.* **105,** 2319–2335.

OLKIN, C. B., L. A. YOUNG, J. L. ELLIOT, D. T. THOLEN. AND M. W. BUIE 1993. Individual light curves of Pluto and Charon. *Bull. Am. Astron. Soc.* **25,** 1132.

OWEN, T. C., T. L. ROUSH, D. P. CRUIKSHANK, J. L. ELLIOT, L. A. YOUNG, C. DE BERGH, B. SCHMITT, T. R. GEBALLE, R. H. BROWN, AND M. J. BARTHOLOMEW 1993. Surface ices and the atmospheric composition of Pluto. *Science* **261,** 745–748.

PRESS, W. H., B. P. FLANNERY, S. A. TEUKOLSKY, AND W. T. VETTERLING 1986. *Numerical Recipes, The Art of Scientific Computing*. Cambridge Univ. Press, Cambridge.

RENSCHEN, C. P. 1977. An interpretation of Pluto's light variation. *Astron. Nachr.* **298,** 179–184.

RODONO, M. 1986. Starspots and plages. In *Highlights in Astronomy* (J.-P. Swings, Ed.), pp. 429–442. D. Reidel Pub. Co., Dordrecht.

ROOT, W. L. 1987. Ill-posedness and precision in object-field reconstruction problems. *J. Opt. Soc. Am.* A4, 171–179.

RUSSELL, H. N. 1906. On the light-variations of satellites and asteroids. *Astrophys. J.* **24,** 1.

SKILLING, J., AND R. K. BRYAN 1984. Maximum entropy image reconstruction: General algorithm. *Mon. Not. R. Astron. Soc.* **211,** 111.

SMITH, W. E., R. G. PAXMAN, AND H. H. BARRETT 1985. Image reconstruction from coded data: I. Reconstruction algorithms and experimental results. *J. Opt. Soc. Am.* A2, 491.

SPEDICATO, E. (Ed.) 1991. *Computer Algorithms for Solving Linear Algebraic Equations, The State of the Art*. Springer-Verlag, Berlin.

STERN, S. A. 1992. The Pluto–Charon system. *Annu. Rev. Astron. Astrophys.* **30,** 185–233.

STERN, S. A. 1993 The Pluto reconnaissance flyby mission. *Eos, Trans. Am. Geophys. Union* **74,** 73–78.

STERN, S. A., L. M. TRAFTON, AND G. R. GLADSTONE 1988. Why is Pluto bright?" Implications of the albedo and lightcurve behavior of Pluto. *Icarus* **75,** 485–498.

THOLEN, D. J., AND E. F. TEDESCO 1984. Photometry of the Pluto–Charon system. *Bull. Am. Astron. Soc.* **16,** 923.

THOMPSON, A. M., AND I. J. D. CRAIG 1992. Automatic strategies for astrophysical inverse problems. *Astron. Astrophys.* **262,** 359–368.

TIKHONOV, A. N., AND A. V. GONCHARSKY 1987. *Ill-Posed Problems in the Natural Sciences*. Mir Publishers, Moscow.

TURCHIN, V. F., V. P. KOZLOV, AND M. S. MALKEVICH 1971. The use of mathematical-statistics methods in the solution of incorrectly posed problems. *Sov. Phys. Uspekhi* **13,** 681.

TWOMEY, S. 1963. On the numerical solution of Fredholm integral equations of the first kind by the inversion of the linear system produced by quadrature. *J. Assoc. Comput. Mach.* **10,** 97.

TWOMEY, S. 1977. *Introduction to the Mathematics of Inversion in Remote Sensing and Indirect Measurements*. Elsevier, New York.

WALKER, M. F., AND R. H. HARDIE 1955. A photometric determination of the rotational period of Pluto. *Publ. Astron. Soc. Pac.* **67,** 224–231.

WILD, W. J. 1989. Matrix formalism for inferring planetary surface albedo distributions from light-curve measurements. *Publ. Astron. Soc. Pac.* **101,** 844–848.

WILD, W. J. 1991. Light-curve inversion formalism. *Astrophys. J.* **368,** 622–625.

WILD, W. J. 1994. *Asteroid Shape and Albedo Imaging via Inversion of the Rotational and Orbital Lightcurves.* In preparation.

WILD. W. J., R. ROSNER, R. HARMON, AND W. F. DRISH, JR., 1994 "Stellar surface mapping by matrix lightcurve inversion", in J.-P. Caillault, Ed. *Cool stars, stellar systems, and the sun* (ASP conference series, Vol. 64) pp. 628–640.

YOUNG, D. M. 1971. *Iterative Solution of Large Linear Systems.* Academic Press, New York.

YOUNG, D. M., AND T.-Z. MAI 1990. The search for omega. In *Iterative Methods for Large Linear Systems.* (D. R. Kincaid and L. J. Hayes, Eds.), pp. 293–311.

YOUNG, E. F. 1992. *An Albedo Map and Frost Model of Pluto.* Ph.D. dissertation, Massachusetts Institute of Technology.

YOUNG, E. F., AND R. P. BINZEL 1989. A surface map for Pluto based on mutual events. *Bull. Am. Astron. Soc.* **21,** 985. [Abstract]

YOUNG, E. F., AND R. P. BINZEL 1990. A singular value decomposition map of Pluto based on mutual event data. *Bull. Am. Astron. Soc.* **22,** 1128. [Abstract]

YOUNG, E. F., AND R. P. BINZEL 1993. Comparative mapping of Pluto's sub-Charon hemisphere: Three least squares models based on mutual event lightcurves. *Icarus* **102,** 134–149.